MATERIALS CHEMISTRY FRONTIERS

CCS 中国化学会 CHINESE CHEMICAL SOCIETY

ICCAS

ROYAL SOCIETY OF CHEMISTRY

# Cation-Intercalation and Conversion-Type Cathode Materials for Rechargeable Aluminum Batteries



| | |
|---|---|
| Journal: | *Materials Chemistry Frontiers* |
| Manuscript ID | QM-REV-09-2021-001267.R1 |
| Article Type: | Review Article |
| Date Submitted by the Author: | 28-Nov-2021 |





| | |
|---|---|
| Complete List of Authors: | Liu, Tianming; China University of Geosciences Beijing School of Science<br>Lv, Guocheng; China University of Geosciences Beijing, School of Materials Science and Technology<br>Liu, Meng; China University of Geosciences Beijing, School of Materials Science and Technology<br>Zhao, Changchun; China University of Geosciences Beijing, School of Science<br>Liao, Libing; China University of Geosciences Beijing, School of Materials Sciences and Technology<br>Liu, Hao; China University of Geosciences Beijing, School of Science<br>Shi, Jiayan; University of California Riverside, Chemical and Environmental Engineering<br>Zhang, Jian; University of California Riverside, Materials Science and Engineering<br>Guo, Juchen; University of California Riverside, Chemical and Environmental Engineering |
| | |

# Cation-Intercalation and Conversion-Type Cathode Materials for Rechargeable Aluminum Batteries

Tianming Liu,[a] Guocheng Lv,[*b] Meng Liu,[b] Changchun Zhao,[*a] Libing Liao,[b] Hao Liu,[a] Jiayan Shi,[c] Jian Zhang,[d] Juchen Guo[*c,d]

[a]*School of Science, China University of Geosciences, Beijing, 100083, China.*
*E-mail: zhaocc@cugb.edu.cn*
[b]*Beijing Key Laboratory of Materials Utilization of Nonmetallic Minerals and Solid Wastes, National Laboratory of Mineral Materials, School of Materials Science and Technology, China University of Geosciences, Beijing 100083, China.*
*E-mail: guochenglv@cugb.edu.cn*
[c]*Department of Chemical and Environmental Engineering,* [d]*Materials Science and Engineering Program, University of California, Riverside, California 92521, United States.*
*E-mail: jguo@engr.ucr.edu*

## Abstract

The current research on cation-intercalation and conversion-type cathode materials for rechargeable aluminum batteries (RABs) is discussed in this critical review. The experimental evidence for $Al^{3+}$ intercalation in transition metal oxides, chalcogenides, MXene, and Prussian blue analogues in both chloroaluminate ionic liquid and aqueous electrolytes is analyzed to identify the true reaction mechanisms. Chevrel phase molybdenum sulfide ($Mo_6S_8$) is the only proven intercalation material for RABs with unambiguous evidence, different understanding of the $Al^{3+}$ intercalation mechanism in $Mo_6S_8$ is discussed. For conversion-type cathode materials, the discussion is focused on the conversion mechanism of metal chalcogenides, and the unique reversible oxidation mechanism of sulfur and selenium enabled by the chloroaluminate ionic liquid electrolytes. The reaction mechanisms of organic cathode materials are also discussed.

## 1. Introduction

Rechargeable aluminum (Al) batteries are considered as an alternative electrochemical energy storage technology for large-scale applications.[1] Despite the low battery voltage due to the high reduction potential of Al (-1.7 V vs. SHE),[2] the high theoretical energy (8046 mAh $cm^{-3}$ and 2981 mAh $g^{-1}$),[3] low cost, and high abundance of Al make rechargeable Al batteries (RABs) worth investigating.[4,5] The majority of the research activities on RABs have been focused on cathode materials, which can be categorized into three groups based on different reaction mechanism: $AlCl_4^-$ intercalation materials, $Al^{3+}$ intercalation materials, and conversion-type materials. $AlCl_4^-$ is the Lewis neutral anion in the benchmark chloroaluminate ionic liquid electrolytes for RABs. It can reversibly intercalate in graphitic carbon materials with excellent current density and cycle life.[6] To date, the $AlCl_4^-$ intercalation cathode materials are overwhelmingly carbon materials including graphite, few-layer graphene, and reduced graphene oxide. The $Al^{3+}$ cation-intercalation and conversion-type cathode materials include a wide variety of materials, of which most are inspired by their application as electrode materials in lithium-ion (Li-ion) batteries. Although the ionic size

of $Al^{3+}$ (0.39 Å) is smaller than that of $Li^{+}$ (0.59 Å), one can expect much more difficult $Al^{3+}$ intercalation due to the large charge density of trivalent $Al^{3+}$ cations. The potential and extent of the conversion reactions in RABs can be also very different from these in Li-ion batteries due to the higher redox potential of $Al^{3+}$/Al. Furthermore, for either $Al^{3+}$ intercalation or conversion, the active specie in the electrolyte is complex chloraluminite anions, which have distinctly different reaction mechanisms from monovalent cations such as $Li^{+}$. In recent years, numerous investigations have been devoted to $Al^{3+}$ intercalation or conversion-type cathode materials for performance improvement and mechanism analysis. However, certain discrepancy still exists in current literature and the mechanisms were not always rigorously validated. This review provides a comprehensive anatomy of the reported intercalation and conversion-type RAB cathode materials with the emphasis on the clarification of reaction mechanisms. It is worth noting that the intercalation-type and conversion-type materials in this review are categorized based on the claims in the publications, not necessarily reflecting their true mechanisms as discussed below.

## 2. $Al^{3+}$ intercalation cathode materials

The intercalation cathode materials can host $Al^{3+}$ cations in their crystal lattice via reversible electrochemical intercalation, and the host lattice must sustain a stable crystal structure. A unique challenge for $Al^{3+}$ intercalation is the strong coulombic interaction between the trivalent $Al^{3+}$ cation and the anionic framework of the host structure. Theoretical calculations indicated that it would be extremely difficult if not impossible for $Al^{3+}$ to intercalate in transition metal oxides or sulfides.[7] Nevertheless, transition metal oxides,[8-13] chalcogenides,[14-18] and their carbon-based composites[19-24] haven been reported as $Al^{3+}$ intercalation cathode materials. It must be pointed out that the $Al^{3+}$ intercalation in the current chloroaluminate ionic liquid electrolytes involves chloroaluminate anions, since there is no simple $Al^{3+}$ cations existing in the electrolytes.

### 2.1 Transition metal oxides

The reported intercalation-type transition metal oxide cathode for RABs include vanadium dioxide ($VO_2$), vanadium pentoxide ($V_2O_5$), lithium vanadate ($Li_3VO_4$), and tin(IV) oxide ($SnO_2$). Wang et al. studied $VO_2$ with metastable monoclinic structure as the host for $Al^{3+}$ intercalation-extraction based on first-principles calculations.[8] The authors simulated that Al occupied the interval of the V-O tunnel in the $VO_6$ octahedron, and increasing the number of x from 0 to 4 in the $[Al_x(V_4O_8)]$ structure. The crystal structure remained stable when the number of intercalated Al was from 0 to 2. However, when 3 or 4 $Al^{3+}$ were inserted, the excessively strong ionic bond would cause serious structural distortion and chemical bonds cleavage. A capacity of 165 mAh $g^{-1}$ in the first discharge was experimentally demonstrated, and it is equivalent to a formula of $Al_{0.17}VO_2$. The capacity retention was 116 mAh $g^{-1}$ after 100 cycles between 0.01 and 0.9 V versus Al under 50 mA $g^{-1}$. Despite the demonstrated performance, unambiguous experimental evidence for the intercalation mechanism was lacking in this study. The X-ray photoelectron spectroscopy (XPS) results indicated the reduction of $V^{4+}$ to $V^{3+}$ after discharge. However, the change of valence state of V cannot validate intercalation mechanism.

Jayaprakash et al. first reported $V_2O_5$ nanowire as an $Al^{3+}$ intercalation cathode for RABs with promising performance.[25] However, a later study by Reed and Menke suggested that the battery-like behavior of the Al-$V_2O_5$ cells could be the result of the electrochemical corrosion of the stainless steel current collector (iron and chromium) in the chloroaluminate ionic liquid electrolyte.[26]

Nevertheless, a number of studies of $V_2O_5$ as the RAB cathode material has been reported in the literature.[9, 10, 12, 25-28] Gu et al. attempted to elucidate the intercalation mechanism and the phase transformation induced by $Al^{3+}$ in $V_2O_5$.[10] The galvanostatic discharge-charge curves in their study shows a stable discharge slope at 0.6 V and a charge slope around 1.0 V versus Al as displayed in Fig. 1a. The XPS indicated that $V^{5+}$ was reduced to $V^{4+}$ during discharge. $V^{3+}$ was detected during the charging process, and it was attributed to the disproportionation. The authors also utilized *ex situ* X-ray diffraction (XRD) to characterize $V_2O_5$ at different stage during discharging and charging (Fig. 1b and c). The XRD results showed shift of the (101) peak and changes of the (001) peak of the orthorhombic $V_2O_5$, which was interpreted as the reversible structural change induced by the $Al^{3+}$ intercalation. However, discrepancies were presented in the study: The galvanostatic intermittent titration technique (GITT) was used to measure the near-equilibrium discharge and charge potentials. The results showed the equilibrium potentials of discharge (intercalation) and charge (extraction) changed drastically along cycling. This observation suggests that the structure of $V_2O_5$ was significantly altered by cycling, which is inconsistent with the intercalation mechanism. The transmission electron microscopic (TEM) characterization revealed amorphous layer on $V_2O_5$ after discharge, indicating irreversible structural change of $V_2O_5$. Finally, the use of nickel (Ni) foam as the current collector is questionable. Shi et al. demonstrated that Ni is not stable in the chloroaluminate ionic liquid electrolyte, and discharge-charge behavior in Al-Ni cell can be obtained due to the corrosion reaction to form active nickel chloride ($NiCl_2$).[29] The complexity of $V_2O_5$ cathode was further revealed by Wen et al, who studied the chemical compatibility between $V_2O_5$ and the chloroaluminate ionic liquids.[30] Their results concluded that $V_2O_5$ chemically reacts to both Lewis neutral $AlCl_4^-$ and Lewis acidic $Al_2Cl_7^-$ anions to produce V-containing electrochemically active species in the electrolyte. Therefore, the feasibility and true reaction mechanism of $V_2O_5$ as the RAB cathode requires further clarification.

$Li_3VO_4$@C composite was demonstrated as a cathode material for RABs with an initial capacity of 137 mAh $g^{-1}$ at a current density of 20 mA $g^{-1}$.[11] *Ex situ* XRD, XPS, $^{27}Al$ nuclear magnetic resonance (NMR), and first-principles calculations were applied to study the $Al^{3+}$ intercalation mechanism in $Li_3VO_4$. The discharge-charge curves and cyclic voltammogram (CV) clearly indicated redox reactions despite lower coulombic efficiency (CE) in the first cycle. The XPS data indicated that the oxidation state of V was reversibly changed between $V^{5+}$ and $V^{4+}$ during discharge and charge. Moreover, the XRD analysis of $Li_3VO_4$ at various stage during the first discharge-charge cycle revealed reversible structural change that was attributed to Al intercalation and extraction. Two possible sites in $Li_3$ chloroaluminate anions crystal structure that can host $Al^{3+}$ cations were proposed (*a*-site and *b*-site shown in Fig. 1d). First-principles calculations indicated that *a*-site is more stable for intercalated $Al^{3+}$ cations (Fig. 1e-f), and the crystal structure change from XRD was consistent with the intercalation of Al into the *a*-site. However, long-term cycling results from XRD clearly indicated deterioration of the crystallinity, resulting in decreased capacity. Although the results and interpretations of this study are self-consistent, the change of the XRD pattern of $Li_3VO_4$ during the first cycle, which was the main evidence of $Al^{3+}$ intercalation, was too subtle to be fully convincing. Interestingly, the $^{27}Al$ NMR spectra indicated that the molar ratio of $AlCl_4^-$ to $Al_2Cl_7^-$ in the electrolyte changed during discharge and charge, which is inconsistent with the conventional assumption that the same amount of chloroaluminate anions would be consumed and generated at the opposite electrodes. A plausible explanation was not provided in this study, however, based on the understanding of the reactions between chloroaluminate anions and $V_2O_5$,[30]

it is possible that the vanadate anion $VO_4^{3-}$ can chemically react with $AlCl_4^-$ and/or $Al_2Cl_7^-$.

Lu et al. reported $SnO_2$ as a cathode material for RABs.[13] Relatively high specific capacity was demonstrated for both $SnO_2$ and it carbon-supported composite as shown in Fig. 1g. The CV curves of $SnO_2$/C show a reduction peak at 0.5 V and an oxidation peak at 0.8 V versus Al, corresponding to the plateau of the galvanostatic discharge and charge curves. XPS spectra show that $Sn^{4+}$ was partially converted to $Sn^{2+}$ during discharge, and then oxidized to $Sn^{4+}$ after charging. *Ex situ* XRD patterns showed the diffraction intensity of $SnO_2$ decreased after discharging and recovered after charging, and the (110) and (001) crystal planes shifted to the left about 0.1° after the charge/discharge process, which is attributed to the increase of the interlayer space (Fig. 1h and i). Unfortunately, the crystallographic evidence of $Al^{3+}$ intercalation was not fully convincing due to the low resolution of the XRD patterns.

Transition metal oxides such as titanium dioxide ($TiO_2$),[31-33] manganese oxides,[34, 35] vanadium oxides,[36, 37] molybdenum trioxide ($MoO_3$),[38, 39] and molybdenum-tantalum oxide[40] were also studied as the $Al^{3+}$ intercalation cathodes in RABs based on aqueous electrolytes, which are either $AlCl_3$, Al trifluoromethanesulfonate ($Al(OTf)_3$), Al sulfate ($Al_2(SO_4)_3$), or Al nitrate ($Al(NO_3)_3$) solutions in water. Although battery-like discharge and charge performance were always demonstrated in these studies, unambiguous evidence of Al intercalation in these transition metal oxides was generally lacking. It is also worth noting that all the aqueous electrolytes used in these studies are very acidic due to the hydronium $H_3O^+$ generated from the hydrolysis of the hydrated $Al^{3+}$ cations. Transition metal oxides are known for reversible electrochemical intercalation of protons as demonstrated in the studies of $V_2O_5$,[41] $TiO_2$,[42] $MoO_3$[43] in acidic electrolytes. Therefore, the true mechanisms of transition metal oxide cathodes in aqueous RABs need further scrutiny and clarification.

**2.2 Spinel or layered transition metal chalcogenides**

Comparing to transition metal oxides, the analogous chalcogenides generally have lower specific capacity and lower potential versus Al. However, they could be better host structures for $Al^{3+}$ intercalation comparing to oxides due to their more polarizable anion framework and larger lattice sites. Therefore, spinel and two-dimensional (2D) layered metal chalcogenides are natural selections due to their proven applications as the hosts for monovalent and divalent cations.[44-52]

The general formula of cubic thiospinel is $AB_2X_4$ (A, B = divalent and trivalent metals, respectively, and X = chalcogen), and the arrangement of X is cubic close packing. The divalent cation is filled in one-eighth of the tetrahedral void, and the trivalent cation is filled in one-half of the octahedral void. Li et al. studied porous $Co_3S_4$ microspheres from solvothermal synthesis as the cathode material for RABs.[17] Co atoms occupy both the tetrahedral and octahedral positions in the $Co_3S_4$ spinel structure. The evaluation of the electrochemical properties of $Co_3S_4$ was performed with polytetrafluororthylene (PTFE) cells and glassy carbon current collectors to avoid the potential side reactions due to the chloroaluminate ionic liquid electrolyte. The first cycling curve displayed very distinct discharge and charge potential plateaus at 0.68 V and 0.88 V versus Al (Fig. 2a), respectively. Flat potential plateaus in discharge and charge curves typically indicate phase transformation of the host crystal structure, thus a strong implication of intercalation mechanism. The CE of the first cycle is only 64%, which was hypothesized as that part of the intercalated $Al^{3+}$ was trapped in the crystal structure due to the strong interaction between $Al^{3+}$ and the sulfide framework. Furthermore, the XRD pattern showed that the peak intensity of the (311) and (400)

planes was reduced and shifted by 0.24° to left after the first discharge (Fig. 2b), which might be attributed to the $Al^{3+}$ intercalation. However, due to the low resolution of the XRD patterns before and after discharge, no crystal structural information could be obtained. The distinct plateaus in the discharge-charge curve disappeared after only 5 cycles, indicating that the $Co_3S_4$ crystal lattice could not sustain repeated discharge and charge process, thus the phase transformation induced by $Al^{3+}$ intercalation was irreversible. It is interesting that the *in situ* Raman spectra of the electrolyte indicated the consumption of the $Al_2Cl_7^-$ anion and generation of the $AlCl_4^-$ anion after discharge; and vice versa after the charging process. This observation is consistent with the finding in the study by Jiang et al. on $Li_3VO_4$,[11] again indicating that the chloroaluminate ionic liquid may be actively involved in the RAB reactions.

Geng et al. reported two type of titanium sulfides (thiospinel $Cu_{0.31}Ti_2S_4$ and layered $TiS_2$) as $Al^{3+}$ intercalation cathode materials for RABs.[15] The spinel $Cu_{0.31}Ti_2S_4$ has an $Fd\bar{3}m$ space group. Assuming the $Cu^{2+}$ position remains unchanged after discharge, the Rietveld refinement of the XRD patterns suggested that 9% of $Al^{3+}$ occupied the same position as $Cu^{2+}$, resulting to a composition of $Al_{0.09}Cu_{0.31}Ti_2S_4$. The Rietveld refinement of the XRD pattern of $TiS_2$ after Al intercalation indicated that the intercalated $Al^{3+}$ cations occupied 11% of the octahedral intercalation position between the $TiS_2$ layers ($Al_{0.11}TiS_2$). The unit cell volume of the Al-intercalated $TiS_2$ is reduced, which was attributed to the strong attraction to the $TiS_2$ layers from the highly charged $Al^{3+}$ cations. The analysis of the GITT discharge at 50 °C showed the diffusion coefficients of Al are $10^{-18}$ to $10^{-20}$ $cm^2$ $s^{-1}$ in $Cu_{0.31}Ti_2S_4$ and $10^{-18}$ to $10^{-19}$ $cm^2$ $s^{-1}$ in $TiS_2$ (Fig. 2c and d). The low diffusion coefficient is Clearly the main obstacle to the Al intercalation in these two sulfides.

Overall, layered $TiS_2$ cathode demonstrated a higher reversible capacity than the cubic spinel $Cu_{0.31}Ti_2S_4$, indicating that the 2D layered structure may be preferable for $Al^{3+}$ intercalation. To date, a number of other 2D transition metal dichalcogenides including vanadium disulfide ($VS_2$),[20] molybdenum disulfide ($MoS_2$)[21] and molybdenum diselenide ($MoSe_2$)[23] have been reported as the cathodes of RABs. Wu et al. reported nanosheet $VS_2$-graphene composite that exhibited a reduction peak at 0.45 V and an oxidation peak at 1.6 V versus Al in CV as displayed in Fig. 3a. The discharge and charge curves of the $VS_2$ cathode are slope-like, and the incorporation of graphene improved the capacity and capacity retention (Fig. 3b and c). *In situ* XRD revealed that the intensity of the (001) and (011) peaks of $VS_2$ were gradually weakened during discharge until diminished at 0.3 V. After charging to 1.7 V, the diffraction peaks re-appeared. *Ex situ* XRD indicated that the intensity of $VS_2$ characteristic peak (001) became lower during the discharge, and slightly shifted to the left, which suggested the layer spacing of (001) was increased. However, the *in situ* and *ex situ* XRD analysis is not fully consistent, and the crystallographic data were not distinct enough to draw conclusion on the crystal structure change. Therefore, it is not clear if the reaction mechanism between $Al^{3+}$ and $VS_2$ is intercalation.

Yang et al. reported $MoS_2$ as the cathode material for RABs.[21] The composite composed of $MoS_2$ and carbon nano-fibers (CNFs) showed two pairs of redox peaks (0.55 and 0.8 V of reduction and 1 and 1.15 V of oxidation versus Al) in the CV curve at 0.5 mV $s^{-1}$, which corresponded well to the plateaus in the discharge-charge curve. The $MoS_2$/CNFs composite exhibited good rate performance, and maintaining a specific capacity of 112 mAh $g^{-1}$ after 50 cycles at 250 mA $g^{-1}$ (Fig. 3d-f). It is worth noting that the distinct plateaus in the discharge-charge curve are consistent with the intercalation-extraction mechanism. The XPS Mo 3d spectra indicated reversible reduction and oxidation of Mo during discharge and charge. The *ex situ* XRD also showed that the (002) plane

disappeared after full discharge and reappeared when charged to 1.8 V, which was interpreted as the evidence of intercalation mechanism. However, the amount and position of intercalated Al could not be determined due to the low crystallinity of the nanosized $MoS_2$.

$MoSe_2$ was also investigated as the cathode for RABs by An and coworkers.[23] The high-resolution transmission electron microscopy (HRTEM) showed that the *d*-spacing of $MoSe_2$ was increased from 6.7 Å to 7.2 Å after full discharge, and it returned to the original state after charging (Fig. 3g). However, the XPS spectra indicated that the oxidation state of Mo was not changed during the discharge and charge (Fig. 3h), which clearly contradicted to the conventional understanding of intercalation mechanism. One possible explanation is that selenium (Se) is the active element in $MoSe_2$ following a conversion mechanism. Interestingly, the Se 3d XPS spectra were not changed neither after discharge and charge. This observation suggests that not only was Se active but also soluble species was produced from the electrochemical reaction of Se. The electrochemical activity of Se in metal selenides in chloroaluminate ionic liquids was demonstrated by a number of studies, which will be discussed in the section of conversion-type cathode materials.

### 2.3 Chevrel phase molybdenum sulfide ($Mo_6S_8$)

In 2015, Geng et al. first reported the Chevrel phase $Mo_6S_8$ as an $Al^{3+}$ intercalation cathode material for RABs. Chevrel phase has a unique crystal structure composed of octahedral Mo atoms in the cubic sulfur anion unit cell. There are two positions in the $Mo_6S_8$ lattice that can allow intercalation of monovalent and divalent cations.[14, 53-58] The first is at the center of the rhombohedron with eight $Mo_6S_8$ vertices (denoted as $Al_1$), and the second is a smaller site at the face center of the rhombohedron (denoted as $Al_2$). The CV scan demonstrated two pairs of cathodic/anodic peaks indicating the two-step electrochemical reaction occurred in the $Mo_6S_8$ electrode. Consistent with the CV scan, the constant current cycling curves showed two distinct potential plateaus during discharge and two plateaus during charge (Fig. 4a and b), which typically implies intercalation mechanism. The most unambiguous evidence of Al intercalation came from the XRD of $Mo_6S_8$ before and after discharge as displayed in Fig. 4c. The XRD pattern after discharge was distinctly different from the pristine $Mo_6S_8$, and the Rietveld refinement revealed that Al indeed intercalated into the two lattice sites aforementioned. Following this original study, the same group performed a more detailed study on the phase transformation of $Mo_6S_8$ induced by Al intercalation. *Ex situ* XRD was performed at different stage of $Al^{3+}$ intercalation in $Mo_6S_8$, and the obtained XRD patterns were analyzed with Rietveld refinement combined with electrochemical and TEM characterizations.[16] The $Al^{3+}$ intercalation initially prefers the larger site of $Al_1$ over the smaller site $Al_2$. However, the preference quickly diminishes because the strong repulsion between $Al^{3+}$ cations force the intercalating $Al^{3+}$ cation into $Al_2$ sites, resulting to equal occupation in these two sites at the end of first discharge plateau. During the second discharge plateau, $Al^{3+}$ cations exclusively intercalate into the larger $Al_1$ sites due to the strong repulsion between the cations.

Lee et al. proposed a different $Al^{3+}$ intercalation mechanism based on *in situ* XRD characterization:[59] $Al^{3+}$ cations intercalate into $Mo_6S_8$ following a two-step phase change reaction as same as the known $Mg^{2+}$ and $Li^+$ intercalation in $Mo_6S_8$.[60-67] $Al^{3+}$ cations first exclusively intercalate in the $Al_1$ site. Once the $Al_1$ sites are fully occupied resulting to a formula of $AlMo_6S_8$ at the end of first discharge plateau, the $Al^{3+}$ cations start to intercalate into the $Al_2$ sites leading to the fully intercalated formula of $Al_{4/3}Mo_6S_8$. Tong et al. further revealed that the S anions in $Mo_6S_8$ also undergo transient redox reaction during Al intercalation and extraction.[18] The two plateaus of the

first discharge curve of $Mo_6S_8$ at 10 mA $g^{-1}$ and 55°C contributed 95 mAh $g^{-1}$ and 35 mAh $g^{-1}$ capacity respectively, corresponding to 1 mole and 1/3 mole $Al^{3+}$ intercalation in $Al_xMo_6S_8$ (Fig. 4d). Electron energy loss spectroscopy (EELS) (Fig. 4e) and X-ray absorption spectroscopy (XAS) (Fig. 4f) were used to analyze the change of valence state of Mo and S during the $Al^{3+}$ intercalation, respectively. In the pristine $Mo_6S_8$, $S^{n-}$ anion is not at the fully reduced state ($0<n<2$). During the first stage of Al intercalation ($Mo_6S_8$ to $AlMo_6S_8$), $S^{n-}$ is fully reduced to $S^{2-}$ and simultaneously Mo is oxidized. During the second stage of Al intercalation ($AlMo_6S_8$ to $Al_{4/3}Mo_6S_8$), Mo is subsequently reduced meanwhile the valence state of $S^{2-}$ remains unchanged. The synergistic redox of Mo and S is correlated to the change of the crystal structure. The XRD analysis indicates the interplanar space of (111) decreases after the first Al intercalation ($AlMo_6S_8$), and then it increases after the further 1/3 Al intercalation ($Al_{4/3}Mo_6S_8$). The change of the interplanar spacing of (111) can be quantified by the Mo-Mo distance ($Mo_1$ to $Mo_5$) in the Mo octahedron as defined in Fig. 4g. The Rietveld refinement of XRD revealed the $Mo_1$-$Mo_5$ bond length in $Al_1Mo_6S_8$ shrinks from the original 2.842 Å to 2.675 Å. When the rest of Al (1/3) was inserted, the bond length increases to 2.709 Å. The change of the $Mo_1$-$Mo_5$ bond length was also confirmed by the measurement with scanning transmission electron microscopy (STEM). As displayed in Fig. 4h to 4j, the $Mo_1$-$Mo_5$ length in the pristine $Mo_6S_8$ is 2.93 Å, which decreases to 2.77 Å after the first Al intercalation, and then increases to 2.82 Å after the further 1/3 Al intercalation.

In addition to the spectroscopic and microscopic techniques described above, solid-state $^{27}Al$ NMR was also used by Jadhav et al. to analyze the $Al^{3+}$ intercalation in $Mo_6S_8$.[68] The quantitative $^{27}Al$ NMR spectra of $Mo_6S_8$ at different discharge and charge stages indicate simultaneous intercalation of $Al^{3+}$ into the $Al_1$ and $Al_2$ sites. This conclusion is consistent with the finding from Geng et al. from their *ex situ* XRD study. The solid-state $^{27}Al$ NMR also revealed the reversible formation of an amorphous layer on the surface of $Mo_6S_8$, which can be related to the desolvation process of chloroaluminate anions. This is a significant finding since the desolvation (breaking the Al-Cl bonds) prior to $Al^{3+}$ intercalation has not been understood in any intercalation-type cathode materials for RABs. It is clear from the studies above that the site occupation dynamics of $Al^{3+}$ intercalation in $Mo_6S_8$ is still not fully understood to date.

**2.4 MXene**

MXene is a new group of 2D carbide or nitride materials derived from the mother MAX phase ($M_{n+1}AX_n$ where $n$ = 1 to 4, M represents early transition metals, A is group 13 or 14 elements, and X is C or N). Typically acidic etching is used to remove the A elements from MAX phase to obtain the MXene with a general formula of $M_{n+1}X_nT_x$, where T represents the surface functional groups such as oxide, fluoride, chloride, and hydroxide resulted from the etching process.[69, 70] MXene materials recently attracted tremendous research efforts in applications such as catalysis and electrochemical energy storage.[71, 72] Beidaghi and coworkers reported $V_2CT_x$ MXene as an Al-intercalation cathode for RABs.[19] The $V_2CT_x$ MXene is a layered vanadium carbide with many different functional groups on the surface, synthesized by etching Al from the $V_2AlC$ MAX phase. At a current density of 10 mA $g^{-1}$ and a voltage range of 0.1-1.8 V, the capacity of the 1st discharge is 178 mAh $g^{-1}$. *Ex situ* XRD showed the weakening of the (0002) peak intensity of $V_2CT_X$ during discharge, and the (0002) peak also shifted to the right by 0.1 Å indicating no phase transition occurs. Moreover, HRTEM images indicated that the interlayer spacing of $V_2CT_X$ is increased by 0.2 Å after discharge. The XPS spectra show reversible change of the vanadium oxidation state between

$V^{4+}$ and $V^{3+}$. Clearly these active V sites are on the surface of $V_2CT_x$ enabled by the functional groups. The $V_2CT_x$ MXene layers were further exfoliated using tetrabutylammonium hydroxide to increase the interlayer spacing by 11.46 Å. The exfoliated $V_2CT_x$ has a high specific capacity of 392 mAh $g^{-1}$ in the first cycle at a current density of 100 mA $g^{-1}$, which should be attributed to the enriched active surface sites containing V with high oxidation state. In principle, MXene materials should not be categorized as $Al^{3+}$ intercalation cathode materials since their electrochemical activity is provided by the surface functional groups resulted from the etching process.

### 2.5 Prussian blue analogues

Prussian blue analogues (PBAs) are three-dimensional open framework structures with large interstitial sites,[73-75] which are capable of accommodating the intercalation of guest ions such as $Li^+$, $Na^+$, $K^+$, $Mg^{2+}$, $Zn^{2+}$, and $Al^{3+}$.[76-83] PBAs were mainly studied as the $Al^{3+}$ intercalation type electrodes in RABs based on aqueous electrolytes similar to the ones used in the studies of transition metal oxide cathodes ($AlCl_3$, $Al(OTf)_3$, $Al_2(SO_4)_3$, and $Al(NO_3)_3$). Reversible discharge and charge behaviors were demonstrated, and the redox of the transition metal centers during discharge and charge was confirmed in these studies. However, evidence of Al intercalation was lacking. Similar to transition metal oxide cathodes, PBA compounds are also known for highly reversible proton intercalation in acidic electrolytes.[84] Furthermore, research shows that same PBA compound had drastically different behavior toward Al intercalation in aqueous electrolyte versus organic electrolyte: Liu et al. reported that copper hexacyanoferrate (CuHCF) nanoparticles in aqueous $Al_2(SO_4)_3$ electrolyte could exhibit reversible intercalation of $Al^{3+}$ in the voltage range of 0.2 to 1.2 V versus saturated calomel reference electrode with a specific capacity of 58.9 mAh $g^{-1}$ at 50 mA $g^{-1}$. On the other hand, Menke and coworkers demonstrated that CuHCF had very low reversible capacity (between 5 and 14 mAh $g^{-1}$) in $Al(OTf)_3$ electrolyte in diglyme within an electrochemical window between 0.1 and 0.7 V versus Al.[85] These discrepancies suggest that the mechanism of PBAs in aqueous RABs requires further investigation.

## 3. Conversion mechanism cathode materials

Unlike intercalation-type cathode materials that require feasible crystal structures, conversion-type cathodes are more straightforward, at least theoretically. Most of the reported cathode materials for RABs to date are conversion-type. The general conversion reaction mechanism, assuming complete conversion, can be expressed in the reaction below[86]:

$$mnAl^{3+} + M_nX_m + 3mne^- \leftrightarrow mAl_nX + nM \quad (1)$$

where M represents the transition metals and X is the anion such as O, S, Se, etc. For example, the transition metals in CuO,[87] $Co_3O_4$,[88] $FeS_2$,[89] NiS,[90] and $Ni_3S_2$[91] electrodes can be reduced to a low valence state after discharge and generating $Al_2O_3$ or $Al_2S_3$; The transition metals in $Ni_2P$,[92] $Co_2P$,[93] $Co_3(PO_4)_2$[94] and $CoSe_2$[95] cathodes will be reduced to zero-valent state during conversion. It must be pointed out that Reaction 1, which is as same as the conversion mechanism in Li-ion batteries, may not always be true in the chloroaluminate ionic liquid electrolytes as discussed below.

### 3.1 Transition metal oxides

CuO porous microspheres from hydrothermal method was reported as a cathode for RABs.[87] A reduction peak at 0.6 V and an oxidation peak of 0.8 V versus Al were detected in the CV curves. However, the charge-discharge curves demonstrate one additional discharge plateau at 0.2 V and

one additional charge plateau at 2.0 V, which were not clearly explained. But one can speculate that the reductive decomposition of the chloroaluminate ionic liquid electrolyte could be the reason for the low discharge plateau, and chlorine generation could be the reaction for the high charging plateau.[29] Monovalent $Cu^{+}$ was detected in the XPS spectra, confirming the reduction of $Cu^{2+}$. The authors claimed $Cu_2O$ and $Al_2O_3$ as the products from the complete discharge to 0.1 V, however, the XRD pattern of the discharge products was inconclusive. Jiao and coworkers reported a metal organic framework (MOF)-derived $Co_3O_4$ polyhedral cathode for RABs.[88] The CV curves demonstrated two reduction peaks at 0.6 V and 0.4 V and one oxidation peak at 0.97 V versus Al. The XPS Co 2p spectra indicated the existence of metallic Co in fully discharged $Co_3O_4$ (at 0.1 V). The XPS Al 2p spectra after discharge displayed the enhancement of the Al peak, which was attributed to the $Al_2O_3$ product.

### 3.2 Transition metal sulfides and selenides

Most of the conversion-type cathode materials for RABs are transition metal sulfides and selenides. Mori et al. studied $FeS_2$ as a cathode material for RABs at 55 °C.[89] The *ex situ* XRD detected the FeS diffraction peak after the discharge of $FeS_2$, and the FeS peak disappeared after full charging. The S *K*-edge XANES spectra indicate that the peak at 2472 eV decreases along discharging, and the S 1s is gradually transformed to the S 3p bond, which is reversed during the charging process (Fig. 5a). On the other hand, no shift is detected in the absorption edge of the Fe *K*-edge XANES spectra (at 7115 eV), indicating that the oxidation state of Fe is unchanged during discharge and charge (Fig. 5b). The isosbestic point at 7130 eV reveals the coexistence of the two iron compounds in the electrode with no presence of metallic iron, which is consistent with the *ex situ* XRD results. Furthermore, S and Al *K*-edge XANES proved the existence of amorphous $Al_2S_3$. Therefore, the conversion reaction mechanism is described as the redox reaction between $S_2^{2-}$ and $S^{2-}$ (i.e., $FeS_2$ and FeS) accompanied by the formation of amorphous $Al_2S_3$. It is worth noting that the authors found that the discharge products $FeS_2$ and $Al_2S_3$ were readily soluble in the chloroaluminate ionic liquid, which would certainly complicate the discharge-charge process.

Zhuang and coworkers reported a binder-free cobalt disulfide and carbon nanofiber composite ($CoS_2$@CNFs) cathode.[96] The XPS analysis indicated that oxidation state of Co in the pristine $CoS_2$ is $Co^{2+}$, and the anion is $S_2^{2-}$ disulfide. Interestingly, $Co^{3+}$ was detected from the XPS spectra after discharge, indicating that $S_2^{2-}$ must be reduced during discharge. Based on the XRD pattern of the discharge product, the authors proposed $AlCo_2S_4$ as the discharge product, although unknown peaks were detected. $Co_9S_8$ is another cobalt sulfide materials being investigated for RABs. Wang and coworker reported a binder-free $Co_9S_8$@CNT-CNF cathode with ultra-long cycle performance.[97] The charge plateau (1.30 V) and discharge plateau (0.95 V) of the charge-discharge curve are consistent with the cathodic and anodic peaks of the CV curve (Fig. 5c). The XPS spectra indicates the reversible redox of Co during discharge and charge. Hu et al. also demonstrated a two-dimensional porous $Co_9S_8$ nanosheets cathode with a capacity of 120 mAh $g^{-1}$ after 250 cycles at 0.2 A $g^{-1}$.[98] However, the electrochemical characteristics of the porous $Co_9S_8$ nanosheets is quite different from the $Co_9S_8$@CNT-CNF reported by Wang as illustrated from the CV scan and the discharge-charge curves displayed in Fig. 5d. It is clear that the detailed mechanism of $Co_9S_8$ needs further clarification.

Wang et al. reported two types of nickel sulfides including $Ni_3S_2$/graphene composite[91] and NiS nanobelts[90] as the cathode materials for RABs. It is worth noting that the $Ni_3S_2$ cathode is

charged first before discharging due to the low valent states of Ni ($Ni^0$ and $Ni^{2+}$ coexist in $Ni_3S_2$). Peculiarly, the first charging curve is a long voltage plateau at 2.0 V versus Al with a capacity two times higher than that of the discharge (Fig. 5e). The XPS Ni 2p spectrum of the charged $Ni_3S_2$ indicates the disappearance of metallic Ni (characteristic peak at 852.8 eV), confirming the oxidization of $Ni^0$ in $Ni_3S_2$. As displayed in Fig. 5f, the S 2p spectrum after charging shows a new peak at 161.4 eV, which is attributed by the authors to a small amount of NiS.[99] Furthermore, the S 2p spectrum after charging indicates reduced population of $S^{2-}$ anion and increased population of oxidized sulfur species. Therefore, the authors speculate that the long charging plateaus is due to the oxidation of $S^{2-}$. The high plateau at 2.0 V also appears in the subsequent cycles, but with lower capacity. It is necessary to point out that the deconvolution of the XPS S 2p spectra in this work has some flaws: S $2p_{1/2}$ and S $2p_{3/2}$ peaks must appear in pair with a fixed peak separation of 1.16 eV and intensity ratio of 0.51. The S 2p spectra shown in Fig. 5f are not rigorously deconvoluted, therefore the interpretation may be questionable. Nevertheless, *ex situ* XRD showed that the charging products contain $Al_2S_3$, $NiCl_2$, and NiS. NiS can be rationalized as the oxidation product of $Ni_3S_2$ (due to the oxidation of $Ni^0$), however the origin of $Al_2S_3$ and $NiCl_2$ is not explained. The TEM images and selected area electron diffraction (SAED) after the reaction showed the transfer of $Ni_3S_2$ to amorphous structure, which is consistent with the conversion-type mechanism and may be the cause of the decrease in capacity. The same group subsequently studied hexagonal NiS nanobelts cathode,[90] which is supposed to be the charging product of $Ni_3S_2$ according to their previous study. Indeed, the demonstrated electrochemical properties of NiS are consistent with $Ni_3S_2$.

Based on the experimental data presented in the two studies above, there is an alternative explanation of the redox mechanism of $Ni_3S_2$ in the chloroaluminate ionic liquid electrolyte: During the charge of $Ni_3S_2$, the metallic Ni is being oxidized to $NiCl_2$ represented by the high changing plateau, which can explain the origin of the $NiCl_2$ identified by XRD. $NiCl_2$ is electrochemically active in the chloroaluminate ionic liquid. Shi et al. demonstrated that metallic Ni foil could function as an active cathode in Al-Ni cells by forming $NiCl_2$ through charge-first cycling.[29]

Wang et al. prepared a hierarchical CuS microsphere cathode for RABs with a reversible capacity of 90 m Ah $g^{-1}$ at a current density of 20 mA $g^{-1}$ after 100 cycles.[100] The XPS Cu 2p spectra demonstrate reversible redox reaction between $Cu^{2+}$ and $Cu^+$ during discharge and charge. The XRD pattern of the discharged electrode indicate the existence of $Cu_2S$ and $Al_2S_3$. The Raman peak of CuS at 473.56 $cm^{-1}$ also shifted to 470.57 $cm^{-1}$ after discharge, indicating the conversion of CuS to $Cu_2S$.[101]

Transition metal selenides were also investigated as the cathode materials for RABs including cobalt selenide-carbon composite (CoSe@C) derived from MOF ZIF-67,[24] cobalt diselenide-carbon composite in a reduced graphene oxide framework ($CoSe_2$-C@rGO),[95] and 3D ordered microporous (3DOM) $CoSe_2$@C also derived from MOF ZIF-67.[102] Despite different chemical composition and structure, these three cobalt selenides demonstrated very similar electrochemical properties, evidenced by the same feature in the charge-discharge curve and CV scan: a distinct charging plateau (or oxidization peak in CV) at approximately 2.0 V versus Al. It is also worth noting that none of the studies clearly stated whether charging (oxidation scan) or discharging (reduction scan) was applied first in their cycling (CV) experiments, which is critical to understand the reaction mechanism. All three studies provided XPS Co 2p spectra after cycling, but they are not fully self-consistent: Co 2p spectrum of CoSe indicated that the valent state of Co ($Co^{2+}$) does not change throughout charge and discharge; while the Co 2p spectra of $CoSe_2$ indicated the existence of

metallic Co after both discharge and charge, which can be confusing, particularly without knowing if $CoSe_2$ was charged first or discharged first. However, what is consistent in all three studies is the XPS Se 3d spectra, which all indicated that Se anions ($Se^{2-}$ in CoSe and $Se_2^{2-}$ in $CoSe_2$) was oxidized in the charging process. The authors of the CoSe study speculated that $Se^{2-}$ anion was oxidized to positive valence state of $Se^{x+}$ (x may be 4 or 6) after charging. Instead, the authors of the 3DOM $CoSe_2$@C study believed that $Se_2^{2-}$ is oxidized to elemental Se. Nevertheless, it seems like redox of Se may be the main contributor to the demonstrated capacity of these cobalt selenides. Elemental Se has been demonstrated to be electrochemically active toward Al in the chloroaluminate ionic liquid electrolyte,[103-106] therefore the working mechanism of cobalt selenides (particularly the role of Co) needs further clarification. It is also worth mentioning that the high potential charge plateau and the corresponding discharge plateau resembles the charge and discharge plateaus from the $AlCl_4^-$ intercalation in graphitic carbon, thus whether $Cl^-$ is involved in the charge and discharge reactions of the cobalt selenides also needs further investigation.

**3.3 Phosphides and phosphate**

Tu et al. studied nickel phosphide-reduced graphene oxide ($Ni_2P$-rGO) nanosheets as the cathode in RABs.[92] The distinct potential plateau of the initial charging curve at 1.9 V was attributed to potential side reactions of the electrolyte. Three oxidation peaks (0.99 V, 1.35 V and 1.80 V) and two reduction peaks (0.53 V and 0.85 V) were detected in the CV scans, corresponding to the multi-step platform of charge and discharge curves. E*x situ* XRD showed that the peak intensity of the $Ni_2P$ was significantly lowered after discharge, and the crystallinity increased after charging. The XPS spectra after discharge indicated the peaks of metallic Ni (853.4 eV and 871.0 eV) and $Ni^{2+}$ (856.2 eV and 874.4 eV). TEM image and SAED after discharge confirmed the formation of the metallic Ni. The change of the valence state of P indicates that $Ni^{2+}$ is partially irreversibly reduced to metallic Ni after discharge.

Lu et al. synthesized a Co-P compound supported on carbon cloth (Co-P/CC) as the cathode for RABs.[93] XRD analysis confirmed the Co-P/CC is composed of polycrystal $Co_2P$ and mellitic Co nanoparticles. The Co-P/CC composite demonstrated higher reversible capacity and lower voltage hysteresis comparing to the commercial crystalline $Co_2P$. The oxidation peak at 1.0 V and two reduction peaks of 0.55 and 0.7 V in CV curves corresponded to the potential plateau of the charge and discharge curve, while the 1.9 V charge plateau (not detected in CV) might be attributed to side reactions of the electrolyte. The XPS spectra showed the binding energy of metallic Co increased slightly (781.2 and 797.0 eV) when discharged to 0.01 V, and the peaks of $Co^{2+}$ (781.2 and 797.0 eV) were detected after charging to 2.4 V, and the peaks of metallic Co disappeared. There was no change in the P 2p spectra, which confirmed that $Co^{2+}$ in Co-P/CC electrode is partially reduced to metallic Co during discharge. In addition, the peak intensity of Al 2p after discharge is increased, and the peak intensity of Cl 2p remained the same before and after discharge. Thus, the Co-P/CC cathode underwent a conversion reaction between $Al^{3+}$ and $Co_2P$ during discharge to generate $Al_mCo_nP$ and a small amount of metallic Co, which in turn was oxidized to $Co_2P$ during the charging process. However, the contribution of the metallic Co in the pristine Co-P/CC composite to the charge/discharge capacity is unknown.

Yin and coworkers reported a cobalt phosphate-carbon composite ($Co_3(PO_4)_2$@C) as the cathode of RABs.[94] This composite was obtained by carbonization of MOF ZIF-67@RF (resorcinol formaldehyde) followed by $NH_4H_2PO_4$ etching and heat treatment. The *in situ* XRD indicated a new

peak (24.7°) was generated during discharge from 1.8 V to 0.9 V, and the peak intensity of (210) plane at 25.9° was reduced. The appearance of the new peak during discharge is attributed to the generation of $Al_mCo_n(PO_4)_2$, and the *in situ* XRD patterns confirm the reappearance of the characteristic peaks of $Co_3(PO_4)_2$ after charging. Moreover, the XPS spectra showed the peak intensity of Co $2p_{1/2}$ and Co $2p_{3/2}$ is reduced after discharge, and the signal of $Co^0$ was detected at 0.5 V. The Co 2p spectrum returned to the argininal state after charging to 2.3 V.

**3.4 Sulfur and selenium electrodes**

The conversion reaction between $Al^{3+}$ and sulfur has a relatively high theoretical potential (about 1.3 V versus Al) and an excellent theoretical specific capacity of 1675 mAh $g^{-1}$.[107, 108] Therefore, sulfur has been regarded as the most promising cathode for RABs. The main changelings of the sulfur cathode in RABs include the high hysteresis of the discharge and charge voltage and the slow reaction kinetics.[109] Transition metals has been demonstrated as effective catalysts for Li-S electrochemical reactions.[110, 111] Similarly, MOF-derived Cu-containing hosts were used as the sulfur host in Al-S batteries to improve the kinetics of sulfur species conversion. Guo et al. reported a S@HKUST-1-C composite cathode decorated with Cu nanoparticles (Fig. 6a).[112] The first discharge capacity reached 1200 mAh $g^{-1}$, and the capacity retention was 460 mAh $g^{-1}$ after 500 cycles under 1 A $g^{-1}$ (Fig. 6b). The same group subsequently reported a ZIF-67 derived Co-containing carbon host matrial for Al-S batteries.[113] The demonstrated capacity retention of the S@Co/C electrode was 500 mAh $g^{-1}$ after 200 cycles at 1 A $g^{-1}$. The CV curve indicated a lower discharge-charge hysteresis of S@Co/C comparing to S@C without the Co, confirming the catalytic effect of the Co content (Fig. 6c and 6d). In addition to the conventional redox reaction sulfur between elemental sulfur and sulfide anion ($S^{2-}$), an unique sulfur redox mechanism in which sulfur can be reversibly oxidized to positive valent state in chloroaluminate ionic liquids was recently demonstrated by Qiao and coworkers.[114] This work demonstrated redox of sulfur in two distinct windows: redox between $S^0$ and $S^{2-}$ with by $Al_2S_3$ as the reduction product and the redox between $S^0$ and $S^{4+}$ with $AlSCl_7$ as the oxidation product (Fig. 6e-f). In situ near-edge X-ray absorption fine structure spectroscopy confirmed $SCl_3^+$ as the intermediate product of the electrochemical oxidation of sulfur. This finding lays the groundwork for high-voltage rechargeable Al-S batteries.

The electrochemical properties of Se and S are considered similar, however Se has a great advantage of being significantly more conductive ($1 \times 10^{-3}$ S $m^{-1}$ of Se versus $0.5 \times 10^{-27}$ S $m^{-1}$ of S). it is interesting that similar to sulfur, Se can also be reversibly oxidized in the chloroaluminate ionic liquid electrolytes. Huang et al. constructed a Se/CMK-3 composite as the cathode for Al-Se batteries,[103] in which it was charged first to 2.3 V versus Al in the charge-discharge tests. The charge product was identified as selenium chloride ($Se_2Cl_2$). Therefore, the electrochemical mechanism is the redox reaction between $Se^0$ and $Se_2^{2+}$. A reversible capacity of 178 mAh $g^{-1}$ at 100 mA $g^{-1}$ was demonstrated for 50 cycles with a nominal discharge voltage of 1.8 V versus Al. Interestingly, Liu et al. studied the redox reaction of the same Se@CMK-3 cathode using a discharge-first protocol with a cut-off charging voltage at 1.5 V versus Al (Fig. 6g).[105] It was found that the reversible redox reaction is between $Se^0$ and $Se^{2-}$ anion with $Al_2Se_3$ as the discharge product. Li et al. reported a Se-carbon nanotube (Se@CT) composite cathode.[104] The reversible Se oxidation was also demonstrated in this study with a capacity of 163 mAh $g^{-1}$ at 500 mA $g^{-1}$ for 200 cycles. However, the authors argued high valence state of Se such as $Se^{4+}$ and $Se^{2+}$ in addition to $Se_2^{2+}$ could be the products of charging, which could lead to higher capacity. It is clear that Se is capable of a wide

range of redox reactions between positive and negative valence states enabled by the chloroaluminate ionic liquid electrolyte. Yan and coworkers demonstrated a selenium/graphene aerogel composite (Se/GA) cathode in $AlCl_3$/triethylamine hydrochloride ionic liquid electrolyte.[106] The authors proved that different electrochemical reactions occur in the two voltage ranges of 0.01 to 1.5 V and 1.0 to 2.3 V versus Al. The 6-electron transfer mechanism of Se ($(Se^{2-}\leftrightarrow Se^{0}\leftrightarrow Se^{4+})$) was demonstrated with a theoretical capacity of 2036 mAh $g^{-1}$. In fact, the Se/GA cathode delivered a specific capacity of 1599 mAh $g^{-1}$ ($Se^{0}\leftrightarrow Se^{4+}$ contributing ~ 970 mAh $g^{-1}$ and $Se^{2-}\leftrightarrow Se^{0}$ contributing ~ 629 mAh $g^{-1}$) at a current density of 100 mA $g^{-1}$, reaching a utilization of 78.5% (Fig. 6h). It is worth noting that the high redox potential (approximately 1.85 and 2.06 V versus Al) between Se and the oxidized Se species are very similar to that of some transition metal selenide cathodes for RABs.[24, 95, 102, 115, 116] The similarity implies that these transition metal selenides may have $Se_x^{2-}$ anions as the active species contributing to the demonstrated reversible capacity.

### 3.5 Organic cathode materials

Organic redox materials have been extensively studied as cathode materials for rechargeable Li-ion batteries. RABs can also potentially benefit from the organic cathodes due to their robust redox mechanisms and high redox potential relative to Al comparing to the inorganic materials. Conducting polymers, specifically polypyrrole and polythiophene, were studied by Hudak as the cathode materials for RABs.[117] It was found that both polymers can be reversibly oxidized and reduced in the chloroaluminate ionic liquid electrolytes with chloroaluminate anions functioning as the dopants for the conducting polymers. Stable specific capacity between 30 to 100 mAh $g^{-1}$ was demonstrated. More recent organic cathodes for RABs are based on the reversible reduction of the quinones and the coordination of chloroaluminate cations, including monovalent $AlCl_2^+$ and divalent $AlCl^{2+}$, to the quinones after reduction. Stoddart and coworkers studied a phenanthrenequinone (PQ) based cathode in a Lewis acidic chloroaluminate ionic liquid electrolyte, and confirming the reversible reduction of the quinone and the coordination of monovalent $AlCl_2^+$ in PQ.[118] This organic cathode demonstrated superior capacity retention and rate capability comparing to typical inorganic cathodes: retaining 53 mAh $g^{-1}$ after 5000 cycles at 2 A $g^{-1}$. Lu and coworker studied a polyimide/MOF composite cathode with a capacity of 73 mAh $g^{-1}$ after 2800 cycles under 1 A $g^{-1}$.[119] Similar reaction mechanism involving monovalent $AlCl_2^+$ was proposed. Dominko and colleagues revealed the redox reaction of anthraquinone (AQ) in the chloroaluminate ionic liquid, and they further developed an anthraquinone-based poly(antraquinonyl sulfide) (PAQS) cathode for RABs.[120] The PAQS cathode demonstrated an initial discharge capacity of 190 mAh $g^{-1}$ at 0.5C and a 60% retention after 500 cycles. The authors proposed that the electrochemical mechanism was the reduction of the quinone accompanied with the coordination of the divalent $AlCl^{2+}$. Choi and coworkers reported a tetradiketone (TDK) macrocyclic molecule, which can reversibly react with $AlCl^{2+}$ to achieve a high initial capacity of 350 mAh $g^{-1}$ and excellent stability of 8000 cycles.[121] Compared with PQ that reacting with the monovalent $AlCl_2^+$, the authors proposed that TDK prefers the coordination with divalent $AlCl^{2+}$ due to its low stabilization after reduction from the lower benzene ring to carbonyl ratio. The DFT calculation of binding energy, calculated IR vibration peaks of TDK, and the achieved specific capacity all supported the hypothesis that TDK coordinated with divalent $AlCl^{2+}$.

## 4. Conclusion and outlook

In summary, a number of challenges exist in the current field of $Al^{3+}$ intercalation and conversion-type cathode materials for RABs. For intercalation-type cathode, Chevrel Phase $Mo_6S_8$ is the only material that has been proven to follow such mechanism with unambiguous evidence. Other Chevrel phase materials can also be expected to host Al via intercalation, however, the low specific capacity (due to high molecular mass) and low intercalation-extraction potential versus Al, their practical value is questionable. Although many intercalation-type materials for monovalent cations have been claimed to be capable of hosting $Al^{3+}$ via intercalation too, unambiguous experimental evidence such as crystallographic data is lacking in current studies. XPS has become a conventional technique to characterize the claimed intercalation-type cathode, however, XPS can only reveal the valence state of surface elements and cannot provide crystal structural information. It is critical for studies on $Al^{3+}$ intercalation materials to show unambiguous crystallographic evidence. Furthermore, the desolvation of chloroaluminate anions during $Al^{3+}$ intercalation must be understood.

We believe most of the reported RAB cathode materials are conversion-type based on our analysis of literature. The conversion mechanism may be straightforward in Li-ion batteries, but it can be complex in RABs due to the involvement of the chloroaluminate ionic liquid electrolytes. The first question that has not been clearly answered is the chemical compatibility of the transition metal oxides, chalcogenides, and phosphides with the ionic liquids. A number of studies clearly demonstrate that some metal oxides and sulfides either dissolve in or react with the chloroaluminate ionic liquids. It is important for the researchers to check the chemical compatibility of the cathode materials prior to the study of their electrochemical properties. Some studies on conversion-type cathodes indicated the existence of metallic transition metal such as Ni or Co, thus it must be realized that these metals can be either corroded or electrochemically active in the ionic liquids. For instance, Ni, Ti, and Cu can be oxidize to form their chloride salts in the charging process in the chloroaluminate ionic liquids, and these chloride salts can be cycled in the charge-discharge tests demonstrating battery-like behavior. The true electrochemical reactions during the cycling of the RABs may not be the intended ones. A good example of this statement is the RABs based aqueous electrolytes. Another question about conversion-type cathodes is the role of chalcogenide anions, particularly selenides. A number of studies suggest that selenide anions can be oxidized (charged) to positive valence state, which would significantly improve the specific of these materials.

Sulfur and selenium are more promising conversion-type cathode materials comparing to the ones based on transition metals due to their clear advantage on capacity. Cycling performance of Al-S batteries has been demonstrated, but the reaction mechanism involving the intermediate products is not fully understood. Analogous reaction mechanism as Li-S batteries cannot be assumed in Al-S due to the chloroaluminate ionic liquid electrolytes. Some interesting electrochemical properties of Al-S and Al-Se batteries have been demonstrated, specifically on the wide redox range of S and Se from negative to positive valence states, which can provide an additional boost to their specific capacity. The current studies suggest that the oxidation of S and Se to the positive valence state is enabled by the chloroaluminate anions (i.e., forming $AlSCl_7$ and $Se_2Cl_2$) featured by a high charging plateau around 2 V versus Al. However, this potential is very close to the chlorine generation potential, particularly on cathodes using carbon materials with high surface area, which can lower the overpotential of chlorine generation. Therefore, it may be possible that the charging products of S or Se at high oxidation state such as $Se_2Cl_2$ is not directly from electrochemical oxidation of $Se^0$, instead, it may be the result from the chemical reaction between

Se and the chlorine generated during the charging process at high potential. The performance degradation of Al-S and Al-Se batteries also originates from the shuttle effect, dissolution of intermediate products in the chloroaluminate ionic liquid electrolytes.[114, 122] How to suppress the shuttle effect is the key to improving the cycle stability of Al-S and Al-Se RABs.

All current studies indicated that the chloroaluminate ionic liquid electrolyte is a universal problem for RABs. Although it is not the focus point of this critical review but it is clear the chloroaluminate ionic liquids are not feasible electrolytes for practical RABs. They are expensive, corrosive, prone to oxidation (chlorine generation), and actively reacting with many cathode materials. Research and development of new Al electrolytes is crucial to the RAB technologies.

## Conflicts of interest

The authors declare no conflict of interest.

## Acknowledgements

This work was supported in part by the National Natural Science Foundation of China (No. 21875223). J. G. acknowledges the support from U.S. National Science Foundation through grant CBET-1751929.

# References


1. Liang, Y.; Dong, H.; Aurbach, D.; Yao, Y., Current status and future directions of multivalent metal-ion batteries. *Nature Energy* **2020,** *5* (9), 646-656.

2. Elia, G. A.; Marquardt, K.; Hoeppner, K.; Fantini, S.; Lin, R.; Knipping, E.; Peters, W.; Drillet, J. F.; Passerini, S.; Hahn, R., An Overview and Future Perspectives of Aluminum Batteries. *Adv Mater* **2016,** *28* (35), 7564-7579.

3. Faegh, E.; Ng, B.; Hayman, D.; Mustain, W. E., Practical assessment of the performance of aluminium battery technologies. *Nature Energy* **2020,** *6* (1), 21-29.

4. Wu, F.; Yang, H.; Bai, Y.; Wu, C., Paving the Path toward Reliable Cathode Materials for Aluminum-Ion Batteries. *Adv Mater* **2019,** *31* (16), e1806510.

5. Ambroz, F.; Macdonald, T. J.; Nann, T., Trends in Aluminium-Based Intercalation Batteries. *Advanced Energy Materials* **2017,** *7* (15), 1602093.

6. Lin, M. C.; Gong, M.; Lu, B.; Wu, Y.; Wang, D. Y.; Guan, M.; Angell, M.; Chen, C.; Yang, J.; Hwang, B. J.; Dai, H., An ultrafast rechargeable aluminium-ion battery. *Nature* **2015,** *520* (7547), 324-328.

7. Rong, Z.; Malik, R.; Canepa, P.; Sai Gautam, G.; Liu, M.; Jain, A.; Persson, K.; Ceder, G., Materials Design Rules for Multivalent Ion Mobility in Intercalation Structures. *Chemistry of Materials* **2015,** *27* (17), 6016-6021.

8. Wang, W.; Jiang, B.; Xiong, W.; Sun, H.; Lin, Z.; Hu, L.; Tu, J.; Hou, J.; Zhu, H.; Jiao, S., A new cathode material for super-valent battery based on aluminium ion intercalation and deintercalation. *Sci Rep* **2013,** *3*, 3383.

9. Wang, H.; Bai, Y.; Chen, S.; Luo, X.; Wu, C.; Wu, F.; Lu, J.; Amine, K., Binder-free $V_2O_5$ cathode for greener rechargeable aluminum battery. *ACS Appl Mater Interfaces* **2015,** *7* (1), 80-84.

10. Gu, S.; Wang, H.; Wu, C.; Bai, Y.; Li, H.; Wu, F., Confirming reversible $Al^{3+}$ storage mechanism through intercalation of $Al^{3+}$ into $V_2O_5$ nanowires in a rechargeable aluminum battery. *Energy Storage Materials* **2017,** *6*, 9-17.

11. Jiang, J.; Li, H.; Huang, J.; Li, K.; Zeng, J.; Yang, Y.; Li, J.; Wang, Y.; Wang, J.; Zhao, J., Investigation of the Reversible Intercalation/Deintercalation of Al into the Novel $Li_3VO_4$@C Microsphere Composite Cathode Material for Aluminum-Ion Batteries. *ACS Appl Mater Interfaces* **2017,** *9* (34), 28486-28494.

12. Wang, H.; Bi, X.; Bai, Y.; Wu, C.; Gu, S.; Chen, S.; Wu, F.; Amine, K.; Lu, J., Open-Structured $V_2O_5{\cdot}nH_2O$ Nanoflakes as Highly Reversible Cathode Material for Monovalent and Multivalent Intercalation Batteries. *Advanced Energy Materials* **2017,** *7* (14), 1602720.

13. Lu, H.; Wan, Y.; Wang, T.; Jin, R.; Ding, P.; Wang, R.; Wang, Y.; Teng, C.; Li, L.; Wang, X.; Zhou, D.; Xue, G., A high performance $SnO_2$/C nanocomposite cathode for aluminum-ion batteries. *Journal of Materials Chemistry A* **2019,** *7* (12), 7213-7220.

14. Geng, L.; Lv, G.; Xing, X.; Guo, J., Reversible Electrochemical Intercalation of Aluminum in $Mo_6S_8$. *Chemistry of Materials* **2015,** *27* (14), 4926-4929.

15. Geng, L.; Scheifers, J. P.; Fu, C.; Zhang, J.; Fokwa, B. P. T.; Guo, J., Titanium Sulfides as Intercalation-Type Cathode Materials for Rechargeable Aluminum Batteries. *ACS Appl Mater Interfaces* **2017,** *9* (25), 21251-21257.

16. Geng, L.; Scheifers, J. P.; Zhang, J.; Bozhilov, K. N.; Fokwa, B. P. T.; Guo, J., Crystal Structure Transformation in Chevrel Phase $Mo_6S_8$ Induced by Aluminum Intercalation. *Chemistry of*

*Materials* **2018,** *30* (23), 8420-8425.

17. Li, H.; Yang, H.; Sun, Z.; Shi, Y.; Cheng, H.-M.; Li, F., A highly reversible $Co_3S_4$ microsphere cathode material for aluminum-ion batteries. *Nano Energy* **2019,** *56*, 100-108.

18. Tong, Y.; Gao, A.; Zhang, Q.; Gao, T.; Yue, J.; Meng, F.; Gong, Y.; Xi, S.; Lin, Z.; Mao, M.; Peng, S.; Wang, X.; Xiao, D.; Su, D.; Luo, Y.; Li, H.; Chen, L.; Suo, L.; Gu, L., Cation-synergy stabilizing anion redox of Chevrel phase $Mo_6S_8$ in aluminum ion battery. *Energy Storage Materials* **2021,** *37*, 87-93.

19. VahidMohammadi, A.; Hadjikhani, A.; Shahbazmohamadi, S.; Beidaghi, M., Two-Dimensional Vanadium Carbide (MXene) as a High-Capacity Cathode Material for Rechargeable Aluminum Batteries. *ACS Nano* **2017,** *11* (11), 11135-11144.

20. Wu, L.; Sun, R.; Xiong, F.; Pei, C.; Han, K.; Peng, C.; Fan, Y.; Yang, W.; An, Q.; Mai, L., A rechargeable aluminum-ion battery based on a $VS_2$ nanosheet cathode. *Phys Chem Chem Phys* **2018,** *20* (35), 22563-22568.

21. Yang, W.; Lu, H.; Cao, Y.; Xu, B.; Deng, Y.; Cai, W., Flexible Free-Standing $MoS_2$/Carbon Nanofibers Composite Cathode for Rechargeable Aluminum-Ion Batteries. *ACS Sustainable Chemistry & Engineering* **2019,** *7* (5), 4861-4867.

22. Zhou, Q.; Wang, D.; Lian, Y.; Hou, S.; Ban, C.; Wang, Z.; Zhao, J.; Zhang, H., Rechargeable aluminum-ion battery with sheet-like $MoSe_2$@C nanocomposites cathode. *Electrochimica Acta* **2020,** *354,* 136677.

23. Feng, X.; Li, J.; Ma, Y.; Yang, C.; Zhang, S.; Li, J.; An, C., Construction of Interlayer-Expanded $MoSe_2$/Nitrogen-Doped Graphene Heterojunctions for Ultra-Long-Cycling Rechargeable Aluminum Storage. *ACS Applied Energy Materials* **2021,** *4* (2), 1575-1582.

24. Xing, W.; Du, D.; Cai, T.; Li, X.; Zhou, J.; Chai, Y.; Xue, Q.; Yan, Z., Carbon-encapsulated CoSe nanoparticles derived from metal-organic frameworks as advanced cathode material for Al-ion battery. *Journal of Power Sources* **2018,** *401*, 6-12.

25. Jayaprakash, N.; Das, S. K.; Archer, L. A., The rechargeable aluminum-ion battery. *Chem Commun (Camb)* **2011,** *47* (47), 12610-12612.

26. Reed, L. D.; Menke, E., The Roles of $V_2O_5$ and Stainless Steel in Rechargeable Al–Ion Batteries. *Journal of The Electrochemical Society* **2013,** *160* (6), A915-A917.

27. Diem, A. M.; Fenk, B.; Bill, J.; Burghard, Z., Binder-Free $V_2O_5$ Cathode for High Energy Density Rechargeable Aluminum-Ion Batteries. *Nanomaterials (Basel)* **2020,** *10* (2), 247.

28. Diem, A. M.; Bill, J.; Burghard, Z., Creasing Highly Porous $V_2O_5$ Scaffolds for High Energy Density Aluminum-Ion Batteries. *ACS Applied Energy Materials* **2020,** *3* (4), 4033-4042.

29. Shi, J.; Zhang, J.; Guo, J., Avoiding Pitfalls in Rechargeable Aluminum Batteries Research. *ACS Energy Letters* **2019,** *4* (9), 2124-2129.

30. Wen, X.; Liu, Y.; Jadhav, A.; Zhang, J.; Borchardt, D.; Shi, J.; Wong, B. M.; Sanyal, B.; Messinger, R. J.; Guo, J., Materials Compatibility in Rechargeable Aluminum Batteries: Chemical and Electrochemical Properties between Vanadium Pentoxide and Chloroaluminate Ionic Liquids. *Chemistry of Materials* **2019,** *31* (18), 7238-7247.

31. Liu, S.; Hu, J. J.; Yan, N. F.; Pan, G. L.; Li, G. R.; Gao, X. P., Aluminum storage behavior of anatase $TiO_2$ nanotube arrays in aqueous solution for aluminum ion batteries. *Energy & Environmental Science* **2012,** *5* (12), 9743-9746.

32. Liu, Y.; Sang, S.; Wu, Q.; Lu, Z.; Liu, K.; Liu, H., The electrochemical behavior of $Cl^-$ assisted $Al^{3+}$ insertion into titanium dioxide nanotube arrays in aqueous solution for aluminum ion

batteries. *Electrochimica Acta* **2014,** *143*, 340-346.

33. Kazazi, M.; Abdollahi, P.; Mirzaei-Moghadam, M., High surface area $TiO_2$ nanospheres as a high-rate anode material for aqueous aluminium-ion batteries. *Solid State Ionics* **2017,** *300*, 32-37.

34. Wu, C.; Gu, S.; Zhang, Q.; Bai, Y.; Li, M.; Yuan, Y.; Wang, H.; Liu, X.; Yuan, Y.; Zhu, N.; Wu, F.; Li, H.; Gu, L.; Lu, J., Electrochemically activated spinel manganese oxide for rechargeable aqueous aluminum battery. *Nat Commun* **2019,** *10* (1), 73.

35. He, S.; Wang, J.; Zhang, X.; Chen, J.; Wang, Z.; Yang, T.; Liu, Z.; Liang, Y.; Wang, B.; Liu, S.; Zhang, L.; Huang, J.; Huang, J.; O'Dell, L. A.; Yu, H., A High‐Energy Aqueous Aluminum-Manganese Battery. *Advanced Functional Materials* **2019,** *29* (45), 1905228.

36. Cai, Y.; Kumar, S.; Chua, R.; Verma, V.; Yuan, D.; Kou, Z.; Ren, H.; Arora, H.; Srinivasan, M., Bronze-type vanadium dioxide holey nanobelts as high performing cathode material for aqueous aluminium-ion batteries. *Journal of Materials Chemistry A* **2020,** *8* (25), 12716-12722.

37. González, J. R.; Nacimiento, F.; Cabello, M.; Alcántara, R.; Lavela, P.; Tirado, J. L., Reversible intercalation of aluminium into vanadium pentoxide xerogel for aqueous rechargeable batteries. *RSC Advances* **2016,** *6* (67), 62157-62164.

38. Lahan, H.; Das, S. K., $Al^{3+}$ ion intercalation in $MoO_3$ for aqueous aluminum-ion battery. *Journal of Power Sources* **2019,** *413*, 134-138.

39. Wang, P.; Chen, Z.; Wang, H.; Ji, Z.; Feng, Y.; Wang, J.; Liu, J.; Hu, M.; Fei, J.; Gan, W.; Huang, Y., A high-performance flexible aqueous Al ion rechargeable battery with long cycle life. *Energy Storage Materials* **2020,** *25*, 426-435.

40. Jin, B.; Hejazi, S.; Chu, H.; Cha, G.; Altomare, M.; Yang, M.; Schmuki, P., A long-term stable aqueous aluminum battery electrode based on one-dimensional molybdenum-tantalum oxide nanotube arrays. *Nanoscale* **2021,** *13* (12), 6087-6095.

41. Zhao, Q.; Liu, L.; Yin, J.; Zheng, J.; Zhang, D.; Chen, J.; Archer, L. A., Proton Intercalation/De-Intercalation Dynamics in Vanadium Oxides for Aqueous Aluminum Electrochemical Cells. *Angew Chem Int Ed Engl* **2020,** *59* (8), 3048-3052.

42. Fleischmann, S.; Sun, Y.; Osti, N. C.; Wang, R.; Mamontov, E.; Jiang, D.-e.; Augustyn, V., Interlayer separation in hydrogen titanates enables electrochemical proton intercalation. *Journal of Materials Chemistry A* **2020,** *8* (1), 412-421.

43. Guo, H.; Goonetilleke, D.; Sharma, N.; Ren, W.; Su, Z.; Rawal, A.; Zhao, C., Two-Phase Electrochemical Proton Transport and Storage in α-$MoO_3$ for Proton Batteries. *Cell Reports Physical Science* **2020,** *1* (10), 100225.

44. Li, C.; Han, X.; Cheng, F.; Hu, Y.; Chen, C.; Chen, J., Phase and composition controllable synthesis of cobalt manganese spinel nanoparticles towards efficient oxygen electrocatalysis. *Nat Commun* **2015,** *6*, 7345.

45. Canepa, P.; Bo, S. H.; Sai Gautam, G.; Key, B.; Richards, W. D.; Shi, T.; Tian, Y.; Wang, Y.; Li, J.; Ceder, G., High magnesium mobility in ternary spinel chalcogenides. *Nat Commun* **2017,** *8* (1), 1759.

46. Yin, L.; Kwon, B. J.; Choi, Y.; Bartel, C. J.; Yang, M.; Liao, C.; Key, B.; Ceder, G.; Lapidus, S. H., Operando X-ray Diffraction Studies of the Mg-Ion Migration Mechanisms in Spinel Cathodes for Rechargeable Mg-Ion Batteries. *J Am Chem Soc* **2021,** *143* (28), 10649-10658.

47. Cai, J.; Wang, Z.; Wu, S.; Han, Y.; Li, J., A Machine Learning Shortcut for Screening the Spinel Structures of Mg/Zn Ion Battery Cathodes with a High Conductivity and Rapid Ion Kinetics. *Energy Storage Materials* **2021,** *42*, 277-285.

48. Saha, S.; Assat, G.; Sougrati, M. T.; Foix, D.; Li, H.; Vergnet, J.; Turi, S.; Ha, Y.; Yang, W.; Cabana, J.; Rousse, G.; Abakumov, A. M.; Tarascon, J.-M., Exploring the bottlenecks of anionic redox in Li-rich layered sulfides. *Nature Energy* **2019,** *4* (11), 977-987.

49. Yun, Q.; Li, L.; Hu, Z.; Lu, Q.; Chen, B.; Zhang, H., Layered Transition Metal Dichalcogenide-Based Nanomaterials for Electrochemical Energy Storage. *Adv Mater* **2020,** *32* (1), e1903826.

50. Chen, J.; Chua, D. H. C.; Lee, P. S., The Advances of Metal Sulfides and In Situ Characterization Methods beyond Li Ion Batteries: Sodium, Potassium, and Aluminum Ion Batteries. *Small Methods* **2020,** *4* (1), 1900648.

51. Li, Y.; Qian, J.; Zhang, M.; Wang, S.; Wang, Z.; Li, M.; Bai, Y.; An, Q.; Xu, H.; Wu, F.; Mai, L.; Wu, C., Co-Construction of Sulfur Vacancies and Heterojunctions in Tungsten Disulfide to Induce Fast Electronic/Ionic Diffusion Kinetics for Sodium-Ion Batteries. *Adv Mater* **2020,** *32* (47), e2005802.

52. Thackeray, M. M., Exploiting the Spinel Structure for Li‐ion Battery Applications: A Tribute to John B. Goodenough. *Advanced Energy Materials* **2021,** *11* (2), 2001117.

53. Wan, L. F.; Perdue, B. R.; Apblett, C. A.; Prendergast, D., Mg Desolvation and Intercalation Mechanism at the Mo6S8 Chevrel Phase Surface. *Chemistry of Materials* **2015,** *27* (17), 5932-5940.

54. Tarascon, J. M.; Disalvo, F. J.; Murphy, D. W.; Hull, G. W.; Rietman, E. A.; Waszczak, J. V., Stoichiometry and physical properties of ternary molybdenum chalcogenides $M_xMo_6X_8$ (X = S, Se; M = Li, Sn, Pb). *Journal of Solid State Chemistry* **1984,** *54* (2), 204-212.

55. Aurbach, D.; Lu, Z.; Schechter, A.; Gofer, Y.; Gizbar, H.; Turgeman, R.; Cohen, Y.; Moshkovich, M.; Levi, E., Prototype systems for rechargeable magnesium batteries. *Nature* **2000,** *407* (6805), 724-727.

56. Lancry, E.; Levi, E.; Gofer, Y.; Levi, M.; Salitra, G.; Aurbach, D., Leaching Chemistry and the Performance of the Mo6S8 Cathodes in Rechargeable Mg Batteries. *Chemistry of Materials* **2004,** *16* (14), 2832-2838.

57. Saha, P.; Jampani, P. H.; Datta, M. K.; Hong, D.; Okoli, C. U.; Manivannan, A.; Kumta, P. N., Electrochemical Performance of Chemically and Solid State-Derived Chevrel Phase $Mo_6T_8$ (T = S, Se) Positive Electrodes for Sodium-Ion Batteries. *The Journal of Physical Chemistry C* **2015,** *119* (11), 5771-5782.

58. Juran, T. R.; Smeu, M., Hybrid density functional theory modeling of Ca, Zn, and Al ion batteries using the Chevrel phase $Mo_6S_8$ cathode. *Phys Chem Chem Phys* **2017,** *19* (31), 20684-20690.

59. Lee, B.; Lee, H. R.; Yim, T.; Kim, J. H.; Lee, J. G.; Chung, K. Y.; Cho, B. W.; Oh, S. H., Investigation on the Structural Evolutions during the Insertion of Aluminum Ions into $Mo_6S_8$ Chevrel Phase. *Journal of The Electrochemical Society* **2016,** *163* (6), A1070-A1076.

60. Aurbach, D.; Gofer, Y.; Lu, Z.; Schechter, A.; Chusid, O.; Gizbar, H.; Cohen, Y.; Ashkenazi, V.; Moshkovich, M.; Turgeman, R.; Levi, E., A short review on the comparison between Li battery systems and rechargeable magnesium battery technology. *Journal of Power Sources* **2001,** *97-98*, 28-32.

61. Levi, M. D.; Gizbar, H.; Lancry, E.; Gofer, Y.; Levi, E.; Aurbach, D., A comparative study of $Mg^{2+}$ and $Li^{+}$ ion insertions into the $Mo_6S_8$ Chevrel phase using electrochemical impedance spectroscopy. *Journal of Electroanalytical Chemistry* **2004,** *569* (2), 211-223.

62. Aurbach, D.; Suresh, G. S.; Levi, E.; Mitelman, A.; Mizrahi, O.; Chusid, O.; Brunelli, M., Progress in Rechargeable Magnesium Battery Technology. *Advanced Materials* **2007,** *19* (23), 4260-

4267.

63. Choi, S. H.; Kim, J. S.; Woo, S. G.; Cho, W.; Choi, S. Y.; Choi, J.; Lee, K. T.; Park, M. S.; Kim, Y. J., Role of Cu in $Mo_6S_8$ and Cu mixture cathodes for magnesium ion batteries. *ACS Appl Mater Interfaces* **2015,** *7* (12), 7016-7024.

64. Chu, H.; Pan, J.; Bai, S.; Ma, Y.; Feng, Y.; Wen, Y.; Yang, Y.; Luo, R.; Chen, A., Carbon coated chevrel phase of $Mo_6S_8$ as anode material for improving electrochemical properties of aqueous lithium-ion batteries. *Electrochimica Acta* **2017,** *258*, 236-240.

65. Mao, M.; Lin, Z.; Tong, Y.; Yue, J.; Zhao, C.; Lu, J.; Zhang, Q.; Gu, L.; Suo, L.; Hu, Y. S.; Li, H.; Huang, X.; Chen, L., Iodine Vapor Transport-Triggered Preferential Growth of Chevrel $Mo_6S_8$ Nanosheets for Advanced Multivalent Batteries. *ACS Nano* **2020,** *14* (1), 1102-1110.

66. Xue, W.; Shi, Z.; Suo, L.; Wang, C.; Wang, Z.; Wang, H.; So, K. P.; Maurano, A.; Yu, D.; Chen, Y.; Qie, L.; Zhu, Z.; Xu, G.; Kong, J.; Li, J., Intercalation-conversion hybrid cathodes enabling Li–S full-cell architectures with jointly superior gravimetric and volumetric energy densities. *Nature Energy* **2019,** *4* (5), 374-382.

67. Li, M.; Liu, T.; Shi, Z.; Xue, W.; Hu, Y. S.; Li, H.; Huang, X.; Li, J.; Suo, L.; Chen, L., Dense All-Electrochem-Active Electrodes for All-Solid-State Lithium Batteries. *Adv Mater* **2021,** *33* (26), e2008723.

68. Jadhav, A. L.; Xu, J. H.; Messinger, R. J., Quantitative Molecular-Level Understanding of Electrochemical Aluminum-Ion Intercalation into a Crystalline Battery Electrode. *ACS Energy Letters* **2020,** *5* (9), 2842-2848.

69. Naguib, M.; Kurtoglu, M.; Presser, V.; Lu, J.; Niu, J.; Heon, M.; Hultman, L.; Gogotsi, Y.; Barsoum, M. W., Two-Dimensional Nanocrystals Produced by Exfoliation of $Ti_3AlC_2$. *Advanced Materials* **2011,** *23* (37), 4248-4253.

70. Naguib, M.; Mochalin, V. N.; Barsoum, M. W.; Gogotsi, Y., 25th Anniversary Article: MXenes: A New Family of Two-Dimensional Materials. *Advanced Materials* **2014,** *26* (7), 992-1005.

71. Ling, Z.; Ren, C. E.; Zhao, M.-Q.; Yang, J.; Giammarco, J. M.; Qiu, J.; Barsoum, M. W.; Gogotsi, Y., Flexible and conductive MXene films and nanocomposites with high capacitance. *Proceedings of the National Academy of Sciences* **2014,** *111* (47), 16676.

72. Anasori, B.; Lukatskaya, M. R.; Gogotsi, Y., 2D metal carbides and nitrides (MXenes) for energy storage. *Nature Reviews Materials* **2017,** *2* (2), 16098.

73. Zhang, L.; Chen, L.; Zhou, X.; Liu, Z., Towards High-Voltage Aqueous Metal-Ion Batteries Beyond 1.5 V: The Zinc/Zinc Hexacyanoferrate System. *Advanced Energy Materials* **2015,** *5* (2), 1400930.

74. Hurlbutt, K.; Wheeler, S.; Capone, I.; Pasta, M., Prussian Blue Analogs as Battery Materials. *Joule* **2018,** *2* (10), 1950-1960.

75. Jiang, L.; Lu, Y.; Zhao, C.; Liu, L.; Zhang, J.; Zhang, Q.; Shen, X.; Zhao, J.; Yu, X.; Li, H.; Huang, X.; Chen, L.; Hu, Y.-S., Building aqueous K-ion batteries for energy storage. *Nature Energy* **2019,** *4* (6), 495-503.

76. Pasta, M.; Wang, R. Y.; Ruffo, R.; Qiao, R.; Lee, H.-W.; Shyam, B.; Guo, M.; Wang, Y.; Wray, L. A.; Yang, W.; Toney, M. F.; Cui, Y., Manganese–cobalt hexacyanoferrate cathodes for sodium-ion batteries. *Journal of Materials Chemistry A* **2016,** *4* (11), 4211-4223.

77. Mizuno, Y.; Okubo, M.; Hosono, E.; Kudo, T.; Zhou, H.; Oh-ishi, K., Suppressed Activation Energy for Interfacial Charge Transfer of a Prussian Blue Analog Thin Film Electrode with Hydrated Ions ($Li^+$, $Na^+$, and $Mg^{2+}$). *The Journal of Physical Chemistry C* **2013,** *117* (21), 10877-10882.

78. Wessells, C. D.; Peddada, S. V.; Huggins, R. A.; Cui, Y., Nickel hexacyanoferrate nanoparticle electrodes for aqueous sodium and potassium ion batteries. *Nano Lett* **2011,** *11* (12), 5421-5425.

79. Chae, M. S.; Heo, J. W.; Kwak, H. H.; Lee, H.; Hong, S.-T., Organic electrolyte-based rechargeable zinc-ion batteries using potassium nickel hexacyanoferrate as a cathode material. *Journal of Power Sources* **2017,** *337*, 204-211.

80. Zhou, A.; Jiang, L.; Yue, J.; Tong, Y.; Zhang, Q.; Lin, Z.; Liu, B.; Wu, C.; Suo, L.; Hu, Y. S.; Li, H.; Chen, L., Water-in-Salt Electrolyte Promotes High-Capacity $FeFe(CN)_6$ Cathode for Aqueous Al-Ion Battery. *ACS Appl Mater Interfaces* **2019,** *11* (44), 41356-41362.

81. Wang, D.; Lv, H.; Hussain, T.; Yang, Q.; Liang, G.; Zhao, Y.; Ma, L.; Li, Q.; Li, H.; Dong, B.; Kaewmaraya, T.; Zhi, C., A manganese hexacyanoferrate framework with enlarged ion tunnels and two‐species redox reaction for aqueous Al-ion batteries. *Nano Energy* **2021,** *84,* 105945.

82. Liu, S.; Pan, G. L.; Li, G. R.; Gao, X. P., Copper hexacyanoferrate nanoparticles as cathode material for aqueous Al-ion batteries. *Journal of Materials Chemistry A* **2015,** *3* (3), 959-962.

83. Ru, Y.; Zheng, S.; Xue, H.; Pang, H., Potassium cobalt hexacyanoferrate nanocubic assemblies for high-performance aqueous aluminum ion batteries. *Chemical Engineering Journal* **2020,** *382,* 122853.

84. Wu, X.; Hong, J. J.; Shin, W.; Ma, L.; Liu, T.; Bi, X.; Yuan, Y.; Qi, Y.; Surta, T. W.; Huang, W.; Neuefeind, J.; Wu, T.; Greaney, P. A.; Lu, J.; Ji, X., Diffusion-free Grotthuss topochemistry for high-rate and long-life proton batteries. *Nature Energy* **2019,** *4* (2), 123-130.

85. Reed, L. D.; Ortiz, S. N.; Xiong, M.; Menke, E. J., A rechargeable aluminum-ion battery utilizing a copper hexacyanoferrate cathode in an organic electrolyte. *Chem Commun (Camb)* **2015,** *51* (76), 14397-400.

86. Zhang, Y.; Liu, S.; Ji, Y.; Ma, J.; Yu, H., Emerging Nonaqueous Aluminum-Ion Batteries: Challenges, Status, and Perspectives. *Adv Mater* **2018,** *30* (38), e1706310.

87. Zhang, X.; Zhang, G.; Wang, S.; Li, S.; Jiao, S., Porous CuO microsphere architectures as high-performance cathode materials for aluminum-ion batteries. *Journal of Materials Chemistry A* **2018,** *6* (7), 3084-3090.

88. Xiao, X.; Wang, M.; Tu, J.; Luo, Y.; Jiao, S., Metal–Organic Framework-Derived $Co_3O_4$@MWCNTs Polyhedron as Cathode Material for a High-Performance Aluminum-Ion Battery. *ACS Sustainable Chemistry & Engineering* **2019,** *7* (19), 16200-16208.

89. Mori, T.; Orikasa, Y.; Nakanishi, K.; Kezheng, C.; Hattori, M.; Ohta, T.; Uchimoto, Y., Discharge/charge reaction mechanisms of $FeS_2$ cathode material for aluminum rechargeable batteries at 55°C. *Journal of Power Sources* **2016,** *313*, 9-14.

90. Yu, Z.; Kang, Z.; Hu, Z.; Lu, J.; Zhou, Z.; Jiao, S., Hexagonal NiS nanobelts as advanced cathode materials for rechargeable Al-ion batteries. *Chem Commun (Camb)* **2016,** *52* (68), 10427-10430.

91. Wang, S.; Yu, Z.; Tu, J.; Wang, J.; Tian, D.; Liu, Y.; Jiao, S., A Novel Aluminum-Ion Battery: Al/$AlCl_3$-[EMIm]Cl/$Ni_3S_2$@Graphene. *Advanced Energy Materials* **2016,** *6* (13), 1600137.

92. Tu, J.; Wang, M.; Xiao, X.; Lei, H.; Jiao, S., Nickel Phosphide Nanosheets Supported on Reduced Graphene Oxide for Enhanced Aluminum-Ion Batteries. *ACS Sustainable Chemistry & Engineering* **2019,** *7* (6), 6004-6012.

93. Lu, S.; Wang, M.; Guo, F.; Tu, J.; Lv, A.; Chen, Y.; Jiao, S., Self-supporting and high-loading hierarchically porous Co-P cathode for advanced Al-ion battery. *Chemical Engineering Journal* **2020,** *389,* 124370.

94. Li, C.; Dong, S.; Wang, P.; Wang, C.; Yin, L., Metal‐Organic Frameworks‐Derived Tunnel Structured $Co_3(PO_4)_2$@C as Cathode for New Generation High‐Performance Al‐Ion Batteries.

*Advanced Energy Materials* **2019,** *9* (41), 1902352.

95. Cai, T.; Zhao, L.; Hu, H.; Li, T.; Li, X.; Guo, S.; Li, Y.; Xue, Q.; Xing, W.; Yan, Z.; Wang, L., Stable $CoSe_2$/carbon nanodice@reduced graphene oxide composites for high-performance rechargeable aluminum-ion batteries. *Energy & Environmental Science* **2018,** *11* (9), 2341-2347.

96. Zhuang, R.; Huang, Z.; Wang, S.; Qiao, J.; Wu, J.-C.; Yang, J., Binder-free cobalt sulfide@carbon nanofibers composite films as cathode for rechargeable aluminum-ion batteries. *Chemical Engineering Journal* **2021,** *409,* 128235.

97. Hu, Y.; Ye, D.; Luo, B.; Hu, H.; Zhu, X.; Wang, S.; Li, L.; Peng, S.; Wang, L., A Binder-Free and Free-Standing Cobalt Sulfide@Carbon Nanotube Cathode Material for Aluminum-Ion Batteries. *Adv Mater* **2018,** *30* (2), 1703824.

98. Hu, Z.; Zhi, K.; Li, Q.; Zhao, Z.; Liang, H.; Liu, X.; Huang, J.; Zhang, C.; Li, H.; Guo, X., Two-dimensionally porous cobalt sulfide nanosheets as a high-performance cathode for aluminum-ion batteries. *Journal of Power Sources* **2019,** *440,* 227147.

99. Buckley, A. N.; Woods, R., Electrochemical and XPS studies of the surface oxidation of synthetic heazlewoodite ($Ni_3S_2$). *Journal of Applied Electrochemistry* **1991,** *21* (7), 575-582.

100. Wang, S.; Jiao, S.; Wang, J.; Chen, H. S.; Tian, D.; Lei, H.; Fang, D. N., High-Performance Aluminum-Ion Battery with CuS@C Microsphere Composite Cathode. *ACS Nano* **2017,** *11* (1), 469-477.

101. Minceva-Sukarova, B.; Najdoski, M.; Grozdanov, I.; Chunnilall, C. J., Raman spectra of thin solid films of some metal sulfides. *Journal of Molecular Structure* **1997,** *410-411*, 267-270.

102. Hong, H.; Liu, J.; Huang, H.; Atangana Etogo, C.; Yang, X.; Guan, B.; Zhang, L., Ordered Macro-Microporous Metal-Organic Framework Single Crystals and Their Derivatives for Rechargeable Aluminum-Ion Batteries. *J Am Chem Soc* **2019,** *141* (37), 14764-14771.

103. Huang, X.; Liu, Y.; Liu, C.; Zhang, J.; Noonan, O.; Yu, C., Rechargeable Aluminum-Selenium Batteries with High Capacity. *Chem Sci* **2018,** *9* (23), 5178-5182.

104. Li, Z.; Liu, J.; Huo, X.; Li, J.; Kang, F., Novel One-Dimensional Hollow Carbon Nanotubes/Selenium Composite for High-Performance Al-Se Batteries. *ACS Appl Mater Interfaces* **2019,** *11* (49), 45709-45716.

105. Liu, S.; Zhang, X.; He, S.; Tang, Y.; Wang, J.; Wang, B.; Zhao, S.; Su, H.; Ren, Y.; Zhang, L.; Huang, J.; Yu, H.; Amine, K., An advanced high energy-efficiency rechargeable aluminum-selenium battery. *Nano Energy* **2019,** *66,* 104159.

106. Zhang, T.; Cai, T.; Xing, W.; Li, T.; Liang, B.; Hu, H.; Zhao, L.; Li, X.; Yan, Z., A rechargeable 6-electron Al–Se battery with high energy density. *Energy Storage Materials* **2021,** *41*, 667-676.

107. Chu, W.; Zhang, X.; Wang, J.; Zhao, S.; Liu, S.; Yu, H., A low-cost deep eutectic solvent electrolyte for rechargeable aluminum-sulfur battery. *Energy Storage Materials* **2019,** *22*, 418-423.

108. Yang, H.; Yin, L.; Liang, J.; Sun, Z.; Wang, Y.; Li, H.; He, K.; Ma, L.; Peng, Z.; Qiu, S.; Sun, C.; Cheng, H. M.; Li, F., An Aluminum-Sulfur Battery with a Fast Kinetic Response. *Angew Chem Int Ed Engl* **2018,** *57* (7), 1898-1902.

109. Cohn, G.; Ma, L.; Archer, L. A., A novel non-aqueous aluminum sulfur battery. *Journal of Power Sources* **2015,** *283*, 416-422.

110. Wang, Y.; Wu, J.; Tang, Y.; Lü, X.; Yang, C.; Qin, M.; Huang, F.; Li, X.; Zhang, X., Phase-Controlled Synthesis of Cobalt Sulfides for Lithium Ion Batteries. *ACS Applied Materials & Interfaces* **2012,** *4* (8), 4246-4250.

111. Zheng, S.; Yi, F.; Li, Z.; Zhu, Y.; Xu, Y.; Luo, C.; Yang, J.; Wang, C., Copper-Stabilized Sulfur-Microporous Carbon Cathodes for Li–S Batteries. *Advanced Functional Materials* **2014,** *24* (26), 4156-4163.

112. Guo, Y.; Jin, H.; Qi, Z.; Hu, Z.; Ji, H.; Wan, L.-J., Carbonized-MOF as a Sulfur Host for Aluminum-Sulfur Batteries with Enhanced Capacity and Cycling Life. *Advanced Functional Materials* **2019,** *29* (7), 1807676.

113. Guo, Y.; Hu, Z.; Wang, J.; Peng, Z.; Zhu, J.; Ji, H.; Wan, L. J., Rechargeable Aluminium-Sulfur Battery with Improved Electrochemical Performance by Cobalt-Containing Electrocatalyst. *Angew Chem Int Ed Engl* **2020,** *59* (51), 22963-22967.

114. Li, H.; Meng, R.; Guo, Y.; Chen, B.; Jiao, Y.; Ye, C.; Long, Y.; Tadich, A.; Yang, Q. H.; Jaroniec, M.; Qiao, S. Z., Reversible electrochemical oxidation of sulfur in ionic liquid for high-voltage Al-S batteries. *Nat Commun* **2021,** *12* (1), 5714.

115. Yao, L.; Ju, S.; Xu, T.; Yu, X., Spatial Isolation-Inspired Ultrafine $CoSe_2$ for High-Energy Aluminum Batteries with Improved Rate Cyclability. *ACS Nano* **2021,** *15* (8), 13662-13673.

116. Li, J.; Liu, W.; Yu, Z.; Deng, J.; Zhong, S.; Xiao, Q.; chen, F.; Yan, D., N-doped C@ZnSe as a low cost positive electrode for aluminum-ion batteries: Better electrochemical performance with high voltage platform of ~1.8 V and new reaction mechanism. *Electrochimica Acta* **2021,** *370,* 137790.

117. Hudak, N. S., Chloraluminate-Doped Conducting Polymers as Positive Electrodes in Rechareable Aluminum Batteries. *J Phys Chem C* **2014**, *118*, 5203-5215.

118. Kim, D. J.; Yoo, D.-J.; Otley, M. T.; Prokofjevs, A.; Pezzato, C.; Owczarek, M.; Lee, S. J.; Choi, J. W.; Stoddart, J. F., Rechargeable aluminium organic batteries. *Nature Energy* **2018,** *4* (1), 51-59.

119. Zhou, J.; Yu, X.; Zhou, J.; Lu, B., Polyimide/metal-organic framework hybrid for high performance Al - Organic battery. *Energy Storage Materials* **2020,** *31*, 58-63.

120. Bitenc, J.; Lindahl, N.; Vizintin, A.; Abdelhamid, M. E.; Dominko, R.; Johansson, P., Concept and electrochemical mechanism of an Al metal anode – organic cathode battery. *Energy Storage Materials* **2020,** *24*, 379-383.

121. Yoo, D. J.; Heeney, M.; Glocklhofer, F.; Choi, J. W., Tetradiketone macrocycle for divalent aluminium ion batteries. *Nat Commun* **2021,** *12* (1), 2386.

122. Yu, X.; Manthiram, A., Electrochemical Energy Storage with a Reversible Nonaqueous Room‐Temperature Aluminum‐Sulfur Chemistry. *Advanced Energy Materials* **2017,** *7* (18), 1700561.

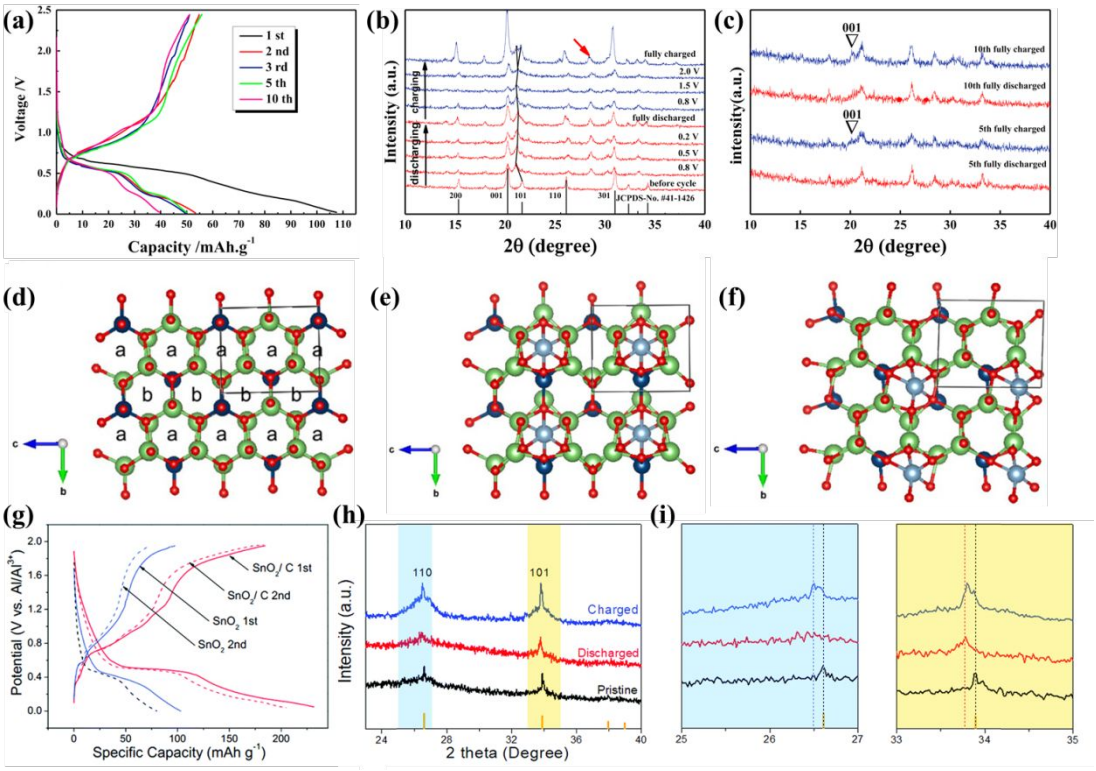


**Fig. 1** (a) Galvanostatic charge-discharge curves of $V_2O_5$ nanowires versus Al under 10 mA $g^{-1}$; (b) *Ex situ* XRD of $V_2O_5$ nanowires during the first cycle at various voltages showing the shift of the (101) peak of orthorhombic $V_2O_5$; (c) *Ex situ* XRD of $V_2O_5$ nanowires after the 5th cycle and 10th cycle showing the change of (001) peak attributed to Al intercalation. Reproduced with permission from ref. 10. Copyright (2017) Elsevier. (d) The optimized crystal structure of $Li_3VO_4$ projected along the a-axis illustrating the a and b sites: Li, green; V, dark blue; O, red; Al, light blue; the structure model of inserting Al into (e) a site and (f) b site. Reproduced with permission from ref. 11. Copyright (2017) American Chemical Society. (g) The 1st and 2nd discharge-charge potential profiles of $SnO_2$ and $SnO_2$/C at 500 mA $g^{-1}$; (h) *Ex situ* XRD of $SnO_2$/C at different stage; (i) Enlarged XRD pattern from (h) showing the shift of (110) and (101) planes. Reproduced with permission from ref. 13. Copyright (2019) The Royal Society of Chemistry.

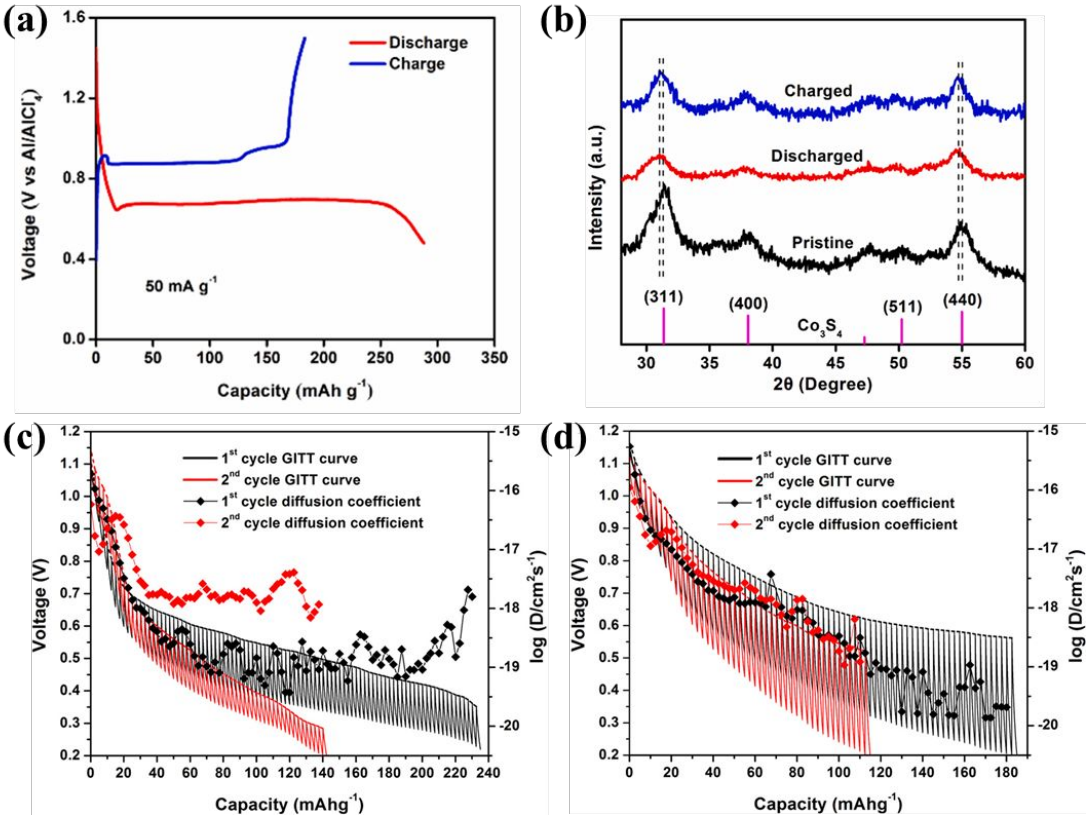


**Fig. 2** (a) The first discharge-charge potential curve of $Co_3S_4$ microspheres versus Al at 50 mA $g^{-1}$; (b) *Ex situ* XRD patterns of $Co_3S_4$ at different charging and discharging states. Reproduced with permission from ref. 17. Copyright (2018) Elsevier. The GITT profiles of (c) $TiS_2$ and (d) $Cu_{0.31}Ti_2S_4$ at 50°C with calculated $Al^{3+}$ diffusion coefficient as the function of capacity (i.e., extent of Al intercalation). Reproduced with permission from ref. 15. Copyright (2017) American Chemical Society.

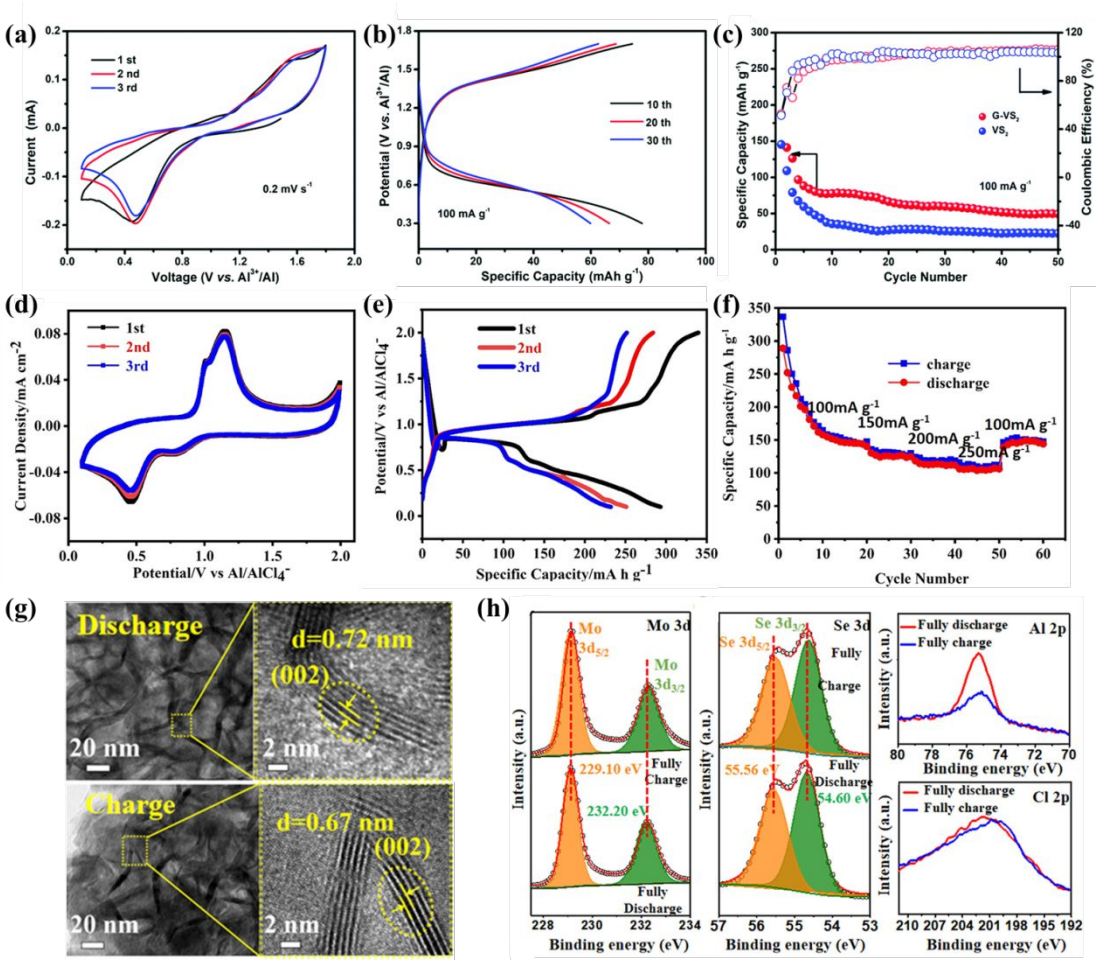


**Fig. 3** (a) The CV curves of the $VS_2$-graphene composite at a scan rate of 0.2 mV $s^{-1}$ versus Al; (b) The 10$^{th}$, 20$^{th}$, and 30th discharge-charge curves of the $VS_2$-graphene composite at a current density of 100 mA $g^{-1}$; (c) Comparison of the cycle stability and CE from $VS_2$ and $VS_2$-graphene at 100 mA $g^{-1}$. Reproduced with permission from ref. 20. Copyright (2018) The Owner Societies. (d) The CV curves of $MoS_2$/CNFs at a scan rate of 0.5 mV $s^{-1}$ versus Al; (e) The discharge-charge curves of $MoS_2$/CNFs at a current density of 100 mA $g^{-1}$; (f) Rate performance of $MoS_2$/CNFs. Reproduced with permission from ref. 21. Copyright (2019) American Chemical Society. (g) HRTEM images of $MoSe_2$ after discharge and charge showing the reversible change of (002) plane spacing; (h) The Mo 3d, Se 3d, Al 2p, and Cl 2p XPS spectra of the fully charged and discharged $MoSe_2$. Reproduced with permission from ref. 23. Copyright (2021) American Chemical Society.

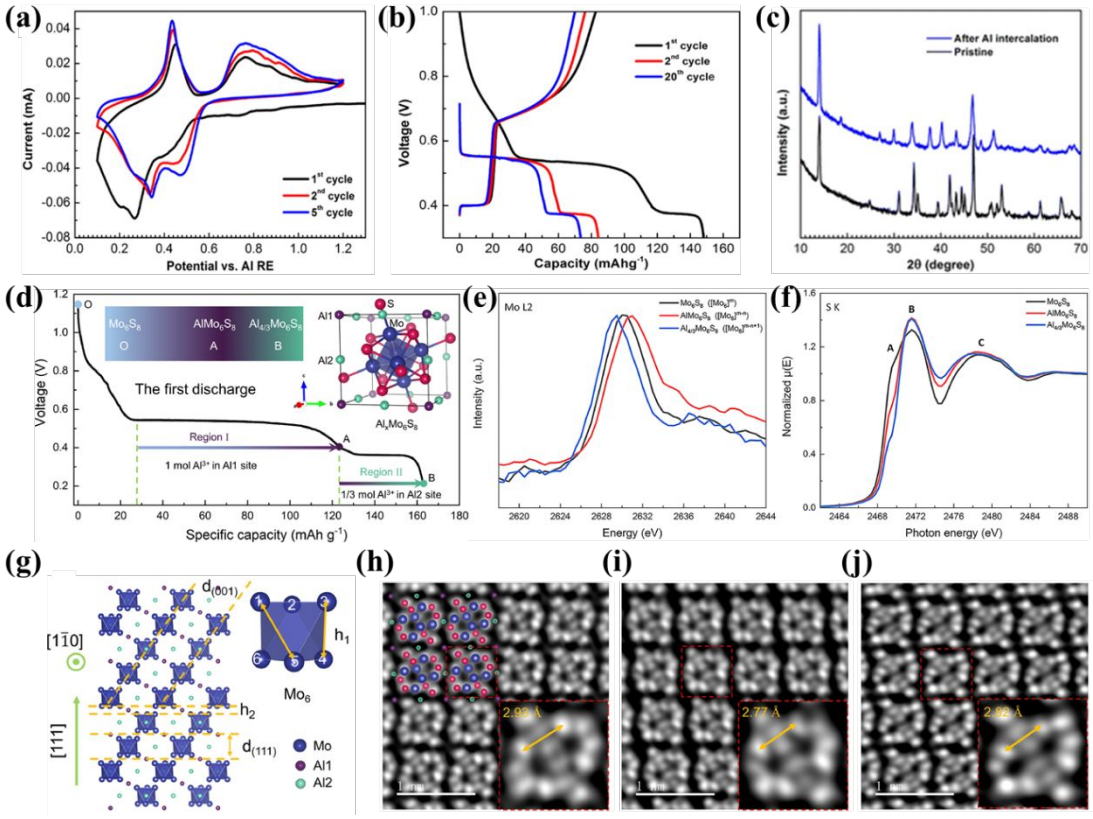


**Fig. 4** (a) The CV curves of $Mo_6S_8$ at 0.1 mV $s^{-1}$ and 50°C; (b) The representative discharge-charge curves of $Mo_6S_8$ at a current density of 12 mA $g^{-1}$ at 50°C; (c) XRD patterns of $Mo_6S_8$ cathode before and after full discharge. Reproduced with permission from ref. 14. Copyright (2015) American Chemical Society. (d) The first discharge profile of $Mo_6S_8$ at 10 mA $g^{-1}$ and 55°C; the insets illustrate the crystal structure of $Al_xMo_6S_8$ and the stages of Al intercalation; (e) Mo *L2*-edge of EELS spectra; (f) S *K*-edge of XAS spectra; (g) The crystal structure of $Mo_6S_8$ along (1$\bar{1}$0) defining the $Mo_1$ to $Mo_5$ distance; (h-j) The STEM images of $Mo_6S_8$, $AlMo_6S_8$, and $Al_{4/3}Mo_6S_8$ along (001) showing the bond length of $Mo_1$-$Mo_5$ varies with Al intercalation, Mo: blue, S: red, $Al_1$: purple, $Al_2$: green. Reproduced with permission from ref. 18. Copyright (2021) Elsevier.

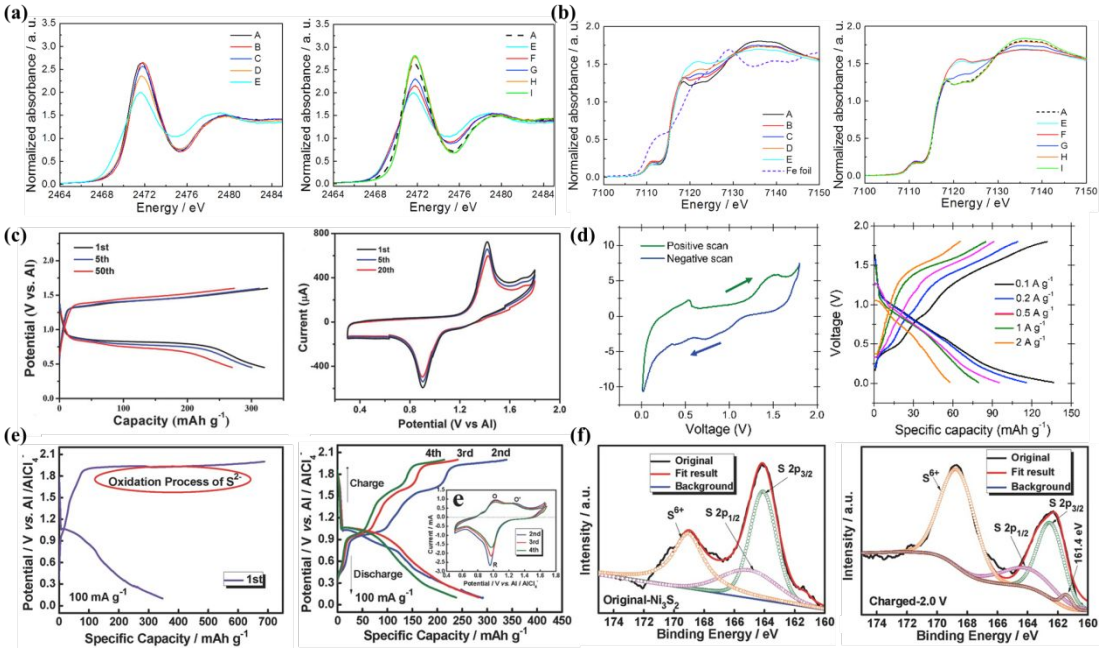


**Fig. 5** (a) S K-edge and (b) Fe K-edge XANES spectra of $FeS_2$ during discharge and charge at 55°C; Potential decreases from A (OCP 1.2 V) to E (0.01 V) during discharge, and increases from E to I (1.8 V) during charge. Reproduced with permission from ref. 89. Copyright (2016) Elsevier. (c) The discharge-charge curves of binder-free $Co_9S_8$@CNT-CNF at 100 mA $g^{-1}$ and CV curves at 0.5 mV $s^{-1}$. Reproduced with permission from ref. 97. Copyright (2017) WILEY. (d) CV curves of $Co_9S_8$ versus Al at a scan rate of 0.25 mV $s^{-1}$ and the discharge-charge curves at different current density. Reproduced with permission from ref. 98. Copyright (2019) Elsevier. (e) The discharge-charge curves of $Ni_3S_2$/graphene at a current density of 100 mA $g^{-1}$; (f) S 2p XPS spectra of $Ni_3S_2$ at the pristine state and after full charge. Reproduced with permission from ref. 91. Copyright (2016) WILEY.

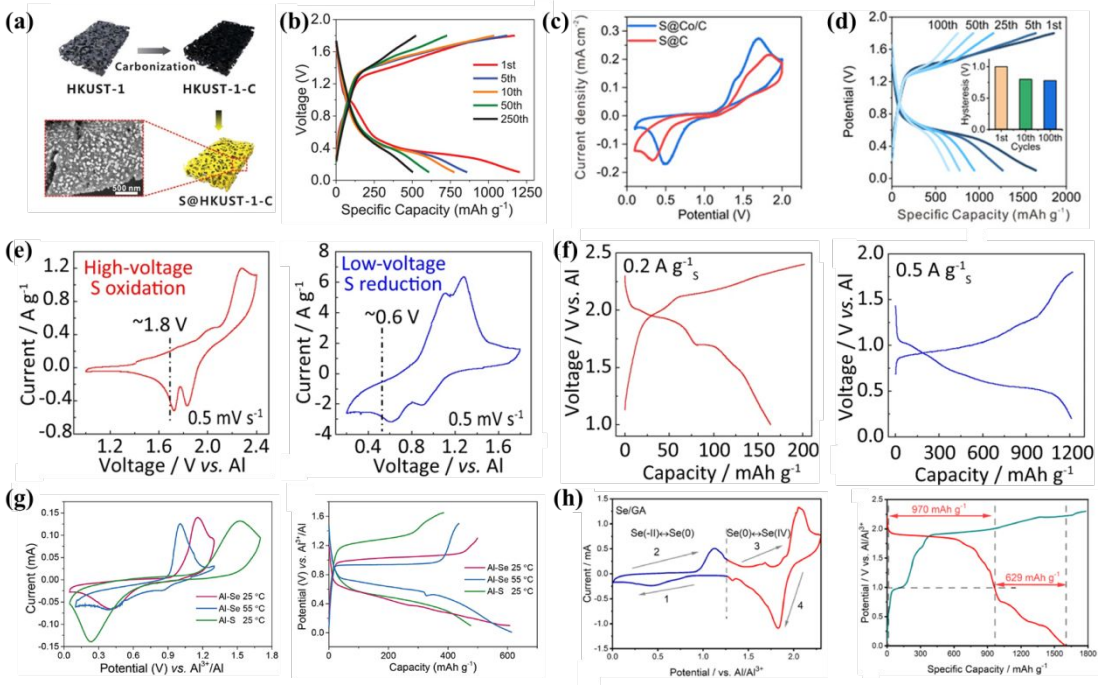


**Fig. 6** (a) Schematic diagram of the synthesis of S@HKUST-1-C; (b) The discharge-charge curves of S@HKUST-1-C at a current density of 1 A $g^{-1}$. Reproduced with permission from ref. 112. Copyright (2018) WILEY. (c) CV curves of S@Co/C and S@C cathodes at 0.2 mV $s^{-1}$; (d) The discharge-charge curves of S@Co/C at 1 A $g^{-1}$; the inset shows the discharge-charge hysteresis at different cycles. Reproduced with permission from ref. 113. Copyright (2020) WILEY. (e) CV curves and (f) discharge-charge potential profiles of S/CNT cathode in electrochemical widows with different cutoff potentials. Reproduced with permission from ref. 114. Copyright (2021) The Author(s). (g) CV scans and the discharge-charge curves of S@CMK-3 and Se@CMK-3 cathodes at 25°C and 55°C. Reproduced with permission from ref. 105. Copyright (2019) Elsevier. (h) CV curves of Se/GA at a scan rate of 0.2 mV $s^{-1}$ and discharge-charge curves at 100 mA $g^{-1}$, the capacity is contributed from the two-stage reaction between $Se^{2-}$ and $Se^{4+}$. Reproduced with permission from ref. 106. Copyright (2021) Elsevier.